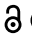




RESEARCH PAPER

 OPEN ACCESS 

OSBPL2 mutations impair autophagy and lead to hearing loss, potentially remedied by rapamycin

Young Ik Koh^{a,†}, Kyung Seok Oh^{a,†}, Jung Ah Kim^a, Byunghwa Noh^b, Hye Ji Choi^b, Sun Young Joo^a, John Hoon Rim^a, Hye-Youn Kim^a, Dong Yun Kim^a, Seyoung Yu^a, Da Hye Kim^b, Sang-Guk Lee^c, Jinsei Jung^b, Jae Young Choi^b, and Heon Yung Gee ^a

^aDepartment of Pharmacology, Graduate School of Medical Science, Brain Korea 21 Project, Yonsei University College of Medicine, Seoul 03722, Republic of Korea; ^bDepartment of Otorhinolaryngology, Graduate School of Medical Science, Brain Korea 21 Project, Yonsei University College of Medicine, Seoul 03722, Republic of Korea; ^cDepartment of Laboratory Medicine, Yonsei University College of Medicine, Seoul Seoul 03722 Republic of Korea

ABSTRACT

Intracellular accumulation of mutant proteins causes proteinopathies, which lack targeted therapies. Autosomal dominant hearing loss (DFNA67) is caused by frameshift mutations in *OSBPL2*. Here, we show that DFNA67 is a toxic proteinopathy. Mutant *OSBPL2* accumulated intracellularly and bound to macroautophagy/autophagy proteins. Consequently, its accumulation led to defective endolysosomal homeostasis and impaired autophagy. Transgenic mice expressing mutant *OSBPL2* exhibited hearing loss, but *osbpl2* knockout mice or transgenic mice expressing wild-type *OSBPL2* did not. Rapamycin decreased the accumulation of mutant *OSBPL2* and partially rescued hearing loss in mice. Rapamycin also partially improved hearing loss and tinnitus in individuals with DFNA67. Our findings indicate that dysfunctional autophagy is caused by mutant proteins in DFNA67; hence, we recommend rapamycin for DFNA67 treatment.

Abbreviations: ABR: auditory brainstem response; ACTB: actin beta; CTSD: cathepsin D; dB: decibel; DFNA67: deafness non-syndromic autosomal dominant 67; DPOAE: distortion product otoacoustic emission; fs: frameshift; GFP: green fluorescent protein; HsQ53R-TG: human p.Q53Rfs*100-transgenic; HEK 293: human embryonic kidney 293; HFD: high-fat diet; KO: knockout; LAMP1: lysosomal associated membrane protein 1; MAP1LC3/LC3: microtubule-associated protein 1 light chain 3; MTOR: mechanistic target of rapamycin kinase; NSHL: non-syndromic hearing loss; OHC: outer hair cells; *OSBPL2*: oxysterol binding protein-like 2; SEM: scanning electron microscopy; SGN: spiral ganglion neuron; SQSTM1/p62: sequestosome 1; TEM: transmission electron microscopy; TG: transgenic; WES: whole-exome sequencing; YUHL: Yonsei University Hearing Loss; WT: wild-type.

ARTICLE HISTORY

Received 12 April 2021
Revised 7 February 2022
Accepted 7 February 2022

KEYWORDS

Autophagy; DFNA67; hearing loss; *OSBPL2*; rapamycin





Introduction

Hearing loss is the most common cause of sensory disorders [1]. Adult-onset hearing loss is more prevalent than childhood-onset hearing loss as the prevalence of hearing loss doubles every 10 years [2]. Approximately 60 loci, and roughly 30 genes identified (<http://hereditaryhearingloss.org/>), are associated with adult-onset hearing loss that is usually inherited in an autosomal dominant manner. Currently, these 30 genes account for only 5 ~ 10% of adult-onset hearing loss cases [2]. Autosomal dominant hearing loss usually manifests as postlingual and progressive hearing loss that begins at high frequencies and leads to deafness throughout all frequencies. Importantly, adult-onset hearing loss constitutes a substantial burden on the adult population worldwide and is associated with higher rates of hospitalization, falls and frailty, depression, and dementia [3–5]. Moreover, hearing loss is becoming an increasingly prevalent disability, due to the global aging


population [6]. However, there are no effective therapeutic strategies for hearing loss so far.

Mutations in *OSBPL2* (oxysterol binding protein like 2; MIM606731) are etiologically linked to the non-syndromic hearing loss (NSHL), deafness non-syndromic autosomal dominant 67 (DFNA67, MIM616340) [7–9]. Individuals with *OSBPL2* mutations develop postlingual hearing loss between ages 5 and 40, as well as bilaterally symmetric, moderate-to-severe hearing loss. Hearing loss starts at high frequencies at an early age and progresses to other frequencies at a later age in most cases.

OSBPL2 belongs to the oxysterol-binding protein (OSBP) family, a group of intracellular lipid receptors [10]. Most members contain an N-terminal pleckstrin homology domain and a highly conserved C-terminal OSBP-like sterol-binding domain, although *OSBPL2* contains only the sterol-binding domain [10]. *In vitro* studies have shown that *OSBPL2* can

CONTACT Jinsei Jung  jsjung@yuhs.ac  Department of Otorhinolaryngology, Graduate School of Medical Science, Brain Korea 21 Project, Yonsei University College of Medicine, Seoul 03722, Republic of Korea; Jae Young Choi  jychoi@yuhs.ac  Department of Otorhinolaryngology, Graduate School of Medical Science, Brain Korea 21 Project, Yonsei University College of Medicine, Seoul, 03722, Republic of Korea; Heon Yung Gee  hygee@yuhs.ac  Department of Pharmacology, Graduate School of Medical Science, Brain Korea 21 Project, Yonsei University College of Medicine, Seoul, 03722, Republic of Korea

[†]These authors contributed equally to this work.

 Supplemental data for this article can be accessed [here](#).

bind to 22- and 25-hydroxycholesterol, phosphatidic acid, and phosphatidylinositol 3-phosphate [11]. *OSBPL2* plays a significant role in the integrated control of cholesterol and triglycerides [11–13], however, the pathogenesis of *OSBPL2* deficiency in NSHL is not fully understood. *OSBPL2*-disrupted pigs display progressive hearing loss with degeneration of cochlear hair cells and morphological abnormalities in stereocilia, as well as hypercholesterolemia [14]. Furthermore, a high-fat diet aggravates the development of hearing loss and leads to more severe hypercholesterolemia. In addition, *OSBPL2* deletion in auditory cells and zebrafish increases cholesterol biosynthesis and drives reactive oxygen species production by inhibiting AMPK activity [15]. Therefore, these studies link dysregulated lipid metabolism resulting from the loss of *OSBPL2*, to hearing impairment. However, how *OSBPL2* mutations lead to hearing loss is still unclear considering that patients have one wild-type and one mutant allele, whereas the investigations only include knockout pigs, cells, and zebrafish models, which show functional defects. This implies that *OSBPL2* mutations may exert a dominant-negative effect rather than haploinsufficiency, but this has not been proven.

Proteinopathy is a term used for any disease caused by abnormal accumulation of misfolded proteins [16]. Protein misfolding and intracellular accumulation are the main features of many human diseases, especially neurodegenerative diseases, including Alzheimer disease, Parkinson disease, amyotrophic lateral sclerosis, prion diseases, and polyglutamine diseases [16]. Some proteinopathies, such as cystic fibrosis resulting from the $\Delta F508$ mutation, are characterized by the accumulation of misfolded proteins in the endoplasmic reticulum (ER) or Golgi apparatus of the secretory pathway [17]. Others involve the accumulation of misfolded protein aggregates in the cytoplasm or the nucleus, such as Lewy bodies in Parkinson disease [18]. Proteinopathy is also one of the causes of genetic hearing loss. The mutations in *SLC26A4*/pendrin result in misfolded *SLC26A4* in the inner ear and lead to congenital deafness due to the degeneration and malformation of the cochlea [19, 20]. In addition, the mutations in *COCH* (cochlin) cause misfolded *COCH* accumulation around the cochlea and slowly deteriorate the hearing function [21, 22].

Here, we identified two *OSBPL2* mutations in families with adult-onset progressive hearing loss, using functional studies to show mutant *OSBPL2* accumulation. We also established a mouse hearing loss model and performed rescue experiments using this model.

Results

Whole-exome sequencing (WES) identified causative *OSBPL2* mutations

At the time of this study, 678 families were enrolled in the Yonsei University Hearing Loss (YUHL) cohort. To identify the genetic cause of hearing loss, we performed WES of 202 families with hearing loss after *GJB2* and *SLC26A4*, the two most commonly mutated genes for hearing loss, were pre-screened [23–25]. Among the 202 families, we detected

potentially causative *OSBPL2* mutations in two families, indicating that 1.0% (2/202) of the hearing loss cases were caused by *OSBPL2*. In these two families, individuals YUHL3 III-13, IV-11, and YUHL457 III-4 were subjected to WES (Figure 1A–B). Based on the pedigrees, autosomal dominant inheritance was suspected in these families (Figure 1A–B). We first examined WES data for nonsynonymous or splice variants in 121 genes known to be linked to hearing loss and found heterozygous frameshift variants in *OSBPL2*; c.158_159AAdel (p.Gln53Argfs*100, p.Q53Rfs*100) in YUHL3 and c.180_181CAdel (p.His60Glnfs*93, p.H60Qfs*93) in YUHL457 (Table 1, Figure 1 A–B, and Fig. S1). We also found that c.180_181CAdel variant has not been reported in any public databases, including dbSNP, EPS, or gnomAD (Table 1). In addition, this variant was also not detected in a whole-genome sequencing dataset of 627 Korean individuals obtained from the National Biobank of Korea and the Centers for Disease Control and Prevention (Table 1). We performed Sanger sequencing to examine whether these *OSBPL2* variants were segregated to the affected status of the two families and found that the variants co-existed in members with the hearing loss phenotype except for YUHL457 IV-6 and V-1, who were in the second and first decade, respectively. (Table 1, Figure 1A–B, and Fig. S1A–B). The c.180_181CAdel (p.H60Qfs*93) variant in *OSBPL2* identified in this study was submitted to ClinVar (accession # SCV001424910).

Patients who had an *OSBPL2* mutation showed symmetric, progressive, and down-sloping sensorineural hearing loss, the onset of which was late teens to twenties (Figure 1C–D and Fig. S2). Although the onset of hearing loss was variable, hearing deterioration did not begin until the early second decade. The severity of hearing loss reached severe-profound hearing loss, whereby patients eventually needed cochlear implantation. The affected individuals in YUHL3 (II-5, III-4, III-13, and IV-11) and YUHL457 (III-4 and III-6) families had cochlear implantation. The outcomes at 3 months after surgery were excellent; open-set auditory hearing was possible, and sentence comprehension score was between 80 and 100%. These findings indicate that the pathology of hearing loss due to *OSBPL2* mutations is favorable for auditory rehabilitation with cochlear implants.

Effect of the identified variants on *OSBPL2* expression

In this study, we found two frameshift mutations, one of which has not been identified before. Therefore, four frameshift mutations were linked to NSHL, and all were two-base pair deletions in exon 3 of *OSBPL2*, which resulted in truncated proteins with the added amino acids almost identical at the same length (Figure 1E–F). We examined whether the frameshift mutations in *OSBPL2* led to decreased *OSBPL2* mRNA expression and observed no difference in the expression of *OSBPL2* mRNA between individuals with and without *OSBPL2* mutation (Figure 1G). Next, to further examine the effect of the identified mutations on *OSBPL2* expression, we performed immunofluorescence assays to visualize wild-type (WT) and mutant *OSBPL2* in HEK 293, HEI-OC1, and HeLa cells. WT *OSBPL2* was diffusely distributed throughout the

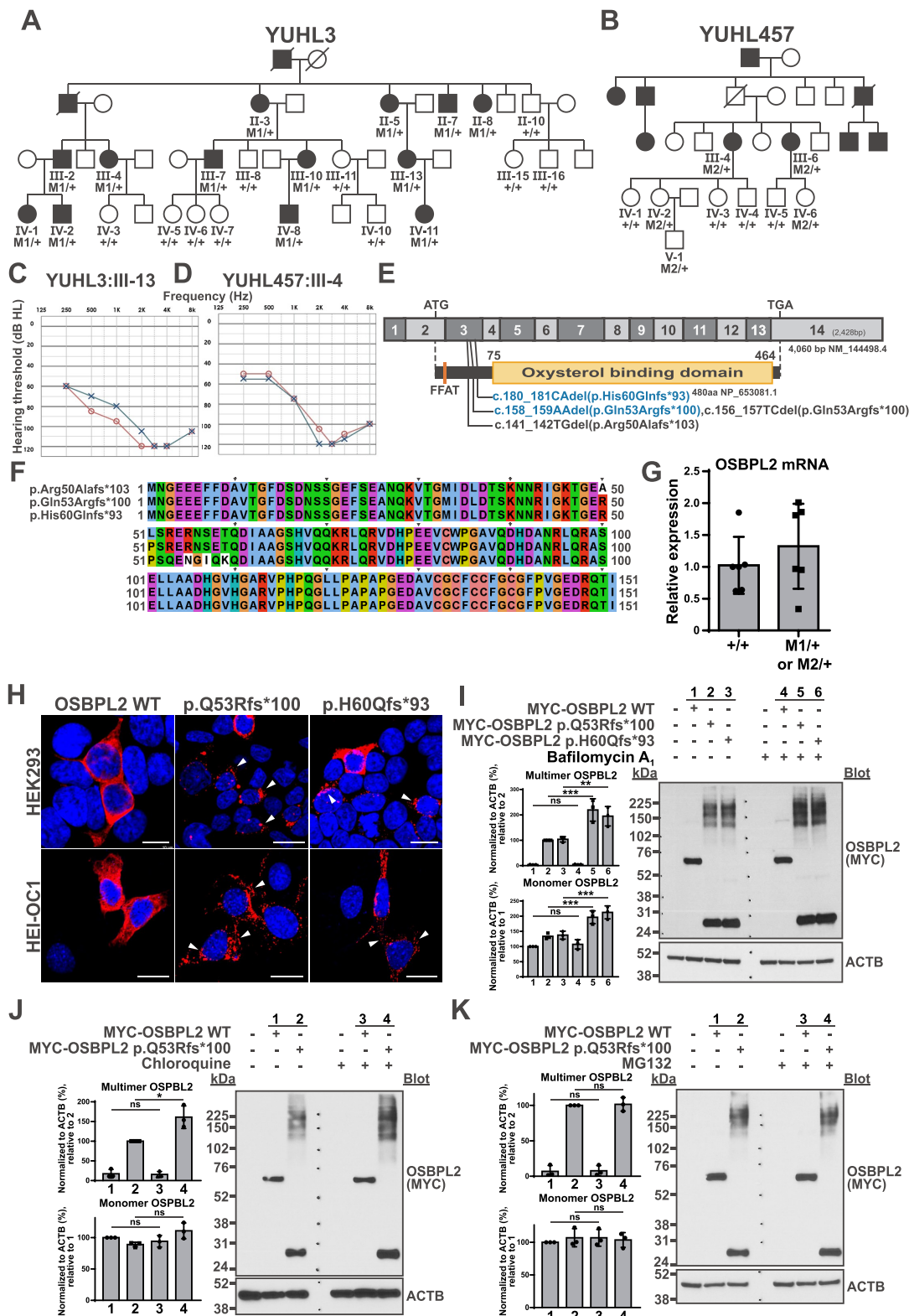


Figure 1. *OSBPL2* mutation identification and *OSBPL2* mutant aggregate formation. (A-B) Pedigrees of the Yonsei University Hearing Loss (YUHL) cohort, families YUHL3 and 457 with an autosomal dominant pattern of hearing loss without syndromic features. *OSBPL2* genotypes of individuals; Sanger sequencing is indicated. M1, c.158_159AAdel (p.Gln53Argfs*100); M2, c.180_181CAdel (p.His60Glnfs*93). (C-D) The pure-tone audiograms of each proband in two affected families showed bilateral sensorineural hearing loss in YUHL3 III-13 (female/37) and YUHL457 III-4 (female/51). The onset of hearing loss was the late 20s and early 30s in YUHL3 III-13 and YUHL457 III-4, respectively. Severe-profound (>70 dB HL) hearing loss mainly affected high frequencies, featuring down-sloping hearing loss. Affected individuals had a residual hearing function at 250 and 500 Hz. Red color, right ear; blue color, left ear. (E) Exon structure of human *OSBPL2* cDNA and domain structure of *OSBPL2*. Frameshift variants identified in individuals with DFNA67 are indicated, and the variants identified in this study are shown in blue. (F) Sequence alignment of truncated *OSBPL2* mutants. *OSBPL2* mutations linked to DFNA67 result in almost identical fusion proteins, approximately 50 amino acids of N-terminal *OSBPL2* and 100 amino acids of neo-peptide. Added amino acids have no homology to any known protein. (G) Real-time PCR demonstrated that the amount of *OSBPL2* mRNA in individuals with *OSBPL2* mutation is not different from that in individuals without *OSBPL2* mutation. M1, c.158_159AAdel (p.Gln53Argfs*100); M2, c.180_181CAdel (p.His60Glnfs*93). (H) Immunofluorescence overexpressed *OSBPL2* wild-type (WT) and mutants in HeLa or HEI-OC1 cells. Cells were immunostained with anti-MYC

cytoplasm in all cell lines (Figure 1H and Fig. S3A). OSBPL2 mutant truncated proteins, p.R50Afs*103, p.Q53Rfs*100, and p.H60Qfs*93, formed cytoplasmic aggregates upon overexpression in all cell lines; however, the missense variant, p.L195M, did not form cytoplasmic aggregates and had similar localization pattern to WT protein (Figure 1H and Fig. S3A). Western blot analysis also revealed multimer bands in cells overexpressing truncated OSBPL2, but not in cells overexpressing WT or p.L195M OSBPL2 (Figure 1I and Fig. S3B), indicating that p.L195M missense variant was probably different from other truncated mutants in the pathogenesis. The band intensity corresponding to the multimer further increased upon treatment with lysosomal inhibitors bafilomycin A₁ or chloroquine, but not with MG132, a proteasomal inhibitor (Figure 1I-K), thus suggesting that multimers of mutant OSBPL2 were degraded by lysosomes. We also compared the stability of WT and mutant OSBPL2 in a heterologous system. HEK 293 cells, overexpressing OSBPL2, were treated with cycloheximide (100 µg/ml) for up to 12 h to block protein synthesis. Western blot analysis showed that cells expressing mutant OSBPL2 had multimer-size bands, which were hardly observed in cells expressing WT OSBPL2, even under denaturing conditions, and that mutant OSBPL2, especially the multimer, was more stable than the WT protein (Figure 2A-D). OSBPL2 is known to form a tetramer [12], therefore, we examined if the truncated mutant protein could still interact with WT OSBPL2 protein even though it lacked the oxysterol-binding domain (Figure 1E). Coimmunoprecipitation showed that p.Q53Rfs*100 could form a dimer with the WT protein (Fig. S4A-B), suggesting that the mutant protein might be dominant-negative.

Further examination of subcellular localization revealed that WT OSBPL2 colocalized with the ER marker, whereas p.Q53Rfs*100 OSBPL2 colocalized with the endosome and lysosome markers (Figure 2E).

Osbp12 knockout mice did not exhibit hearing loss

We confirmed the ubiquitous expression of OSBPL2 in the murine inner ear, including inner and outer hair cells, supporting cells, ganglion neuronal cells, and epithelia of stria vascularis (Figure 3A).

As heterozygous OSBPL2 mutations might have led to autosomal dominant hearing loss via haploinsufficiency or a dominant-negative effect, we first generated *osbp12* knockout (KO, *osbp12*^{-/-}) mice using the CRISPR-Cas9 system. The guide RNA was designed to target exon 3 of *Osbp12* (Figure 3B) as the frameshift mutations identified in humans occurred in the exon 3 of OSBPL2 (Table 1), and resulting edited alleles were screened using the T7E1 assay (Fig. S5A). *Osbp12* targeting was confirmed via genotyping and Western blot analysis (Fig. S5B-C). *osbp12*^{-/-} mice were viable, fertile, and born at an expected Mendelian ratio.

Osbp12^{+/-} and *osbp12*^{-/-} mice were not grossly different from their WT siblings. We determined the hearing sensitivity of *Osbp12*^{+/-} and *osbp12*^{-/-} mice by measuring the auditory brainstem response (ABR) thresholds in response to click stimuli of mixed broadband or pure-tone sounds at individual frequencies up to postnatal day (P) 180 at 30-day intervals. ABR thresholds of both click and pure-tone stimuli at all frequencies in *Osbp12*^{+/-} and *osbp12*^{-/-} mice were comparable to those in *Osbp12*^{+/+} mice (Figure 3C and Fig. S5D). Distortion product otoacoustic emission (DPOAE) thresholds, which reflected the cochlear amplification function of outer hair cells (OHCs), did not significantly differ among any of the genotypes (Figure 3D). Whole-mount immunofluorescence and scanning electron microscopy (SEM) further showed that the stereociliary bundles of OHCs in *Osbp12*^{+/-} and *osbp12*^{-/-} mice were comparable to those in *Osbp12*^{+/+} mice on P120 (Fig. S5E). Histology and immunofluorescence revealed that overall cochlear morphology and spiral ganglion neurons (SGNs) were not different among different genotypes (Figure 3E). In the pig model, high-fat diet (HFD) aggravated the development of hearing loss [14]; therefore, we examined whether HFD induced hearing loss in *Osbp12*^{+/-} and *osbp12*^{-/-} mice. However, *Osbp12*^{+/-} and *osbp12*^{-/-} mice did not show hearing loss or any morphological change upon HFD after weaning up to 16 weeks (Figure 4A-C). In addition, hypercholesterolemia was not observed in *osbp12*^{-/-} mice fed HFD for two months (Figure 4D), and triglyceride, high-density lipoprotein, food uptake, activity, bodyweight, fat composition, and energy expenditure of *Osbp12*^{+/-} and *osbp12*^{-/-} mice were overall similar to those of *Osbp12*^{+/+} mice (Figure 4D and Fig. S6A-E). We also examined the serum lipid profile in individuals with or without a heterozygous OSBPL2 mutation. Individuals with a heterozygous c.158_159AAdel in OSBPL2 had normal lipid and lipoprotein levels similar to control individuals without the allele (Figure 5A-F), indicating that hearing loss in these individuals was not due to abnormal lipid metabolism. These findings did not only suggest that the function of OSBPL2 was not essential for normal hearing, but also excluded haploinsufficiency or a dominant-negative effect as neither *Osbp12*^{+/-} or *osbp12*^{-/-} mice developed hearing loss.

Transgenic mouse model expressing p.Q53Rfs*100 recapitulated hearing loss

As *osbp12*^{-/-} mice did not exhibit hearing loss and hypercholesterolemia, we assumed that truncated OSBPL2 might gain additional functions, which was not observed with WT OSBPL2. To examine this, we considered a knock-in mouse model in which the frameshift mutation identified in human patients is introduced or a transgenic mouse model which expresses human mutant

Table 1. OSBP/L2 mutations detected in individuals with non-syndromic hearing loss using whole-exome sequencing.

Individual	Sex	Age of onset (years)	Nucleotide change ^a	Amino acid change ^b	Exon ^a	Zygosity	dbSNP ^b	ESP ^c	gnomAD ^d	KRGDB ^e	PP2 ^f	MT ^g	Condel ^h	SIFT ⁱ	CADD ^j	HGMMD ^k
YUHL3			c.158_159AAdel	p.Gln53ArgfsTer100	Mar-14	Het	ND	ND	ND	ND	ND	ND	ND	ND	ND	Reported
II-3	F	Mid 20s														
II-5	F	Mid 30s														
II-7	M	Early 20s														
II-8	F	Early 20s														
III-2	M	Early 30s														
III-4	F	Mid 20s														
III-7	F	Early 30s														
III-10	F	Late 20s														
III-13	F	Late 20s														
IV-1	F	Mid 20s														
IV-2	M	Late 10s														
IV-8	M	Late 10s														
IV-11	F	Early 10s														
YUHL457			c.180_181CA del	p.His60fs*93	Mar-14	Het	ND	ND	ND	ND	Dam -0.989	DC -1	Del -0.884	Del 0	29.8	ND
III-4	F	Early 40s														
III-6	F	Early 30s														
IV-2	F	Late 20s														
IV-6	F	-														
V-1	M	-														

Dam, probably damaging; Del, deleterious; DC, disease-causing; Het, heterozygous in the affected individual; F, female; M, male; ND, no data.

^acDNA mutations are numbered according to human cDNA reference sequence NM_144498.2 (OSBP/L2); +1 corresponds to the A of the ATG translation initiation codon.

^bdbSNP database (<http://www.ncbi.nlm.nih.gov/SNP>).

^cNHLBI Exome Sequencing Project (<http://evs.gs.washington.edu/EVS/>).

^dgnomAD browser (<http://exac.broadinstitute.org/>).

^eThe Korean Reference Genome Database.

^fPolyPhen-2 HumVar prediction score (<http://genetics.bwh.harvard.edu/pph2/>).

^gMutation taster (<http://www.mutationtaster.org/>).

^hCondel (<http://bbglab.irbbarcelona.org/fannsd/b/>).

ⁱSIFT, Sorting Intolerant from Tolerant (<http://sift.jcvi.org/>).

^jCADD, Phred-like scores (scaled C scores) on Combined Annotation Dependent Depletion (<http://cadd.gs.washington.edu/home/>).

^kHGMMD, The Human Gene Mutation Database (<http://www.hgmd.cf.ac.uk/ac/index.php>).

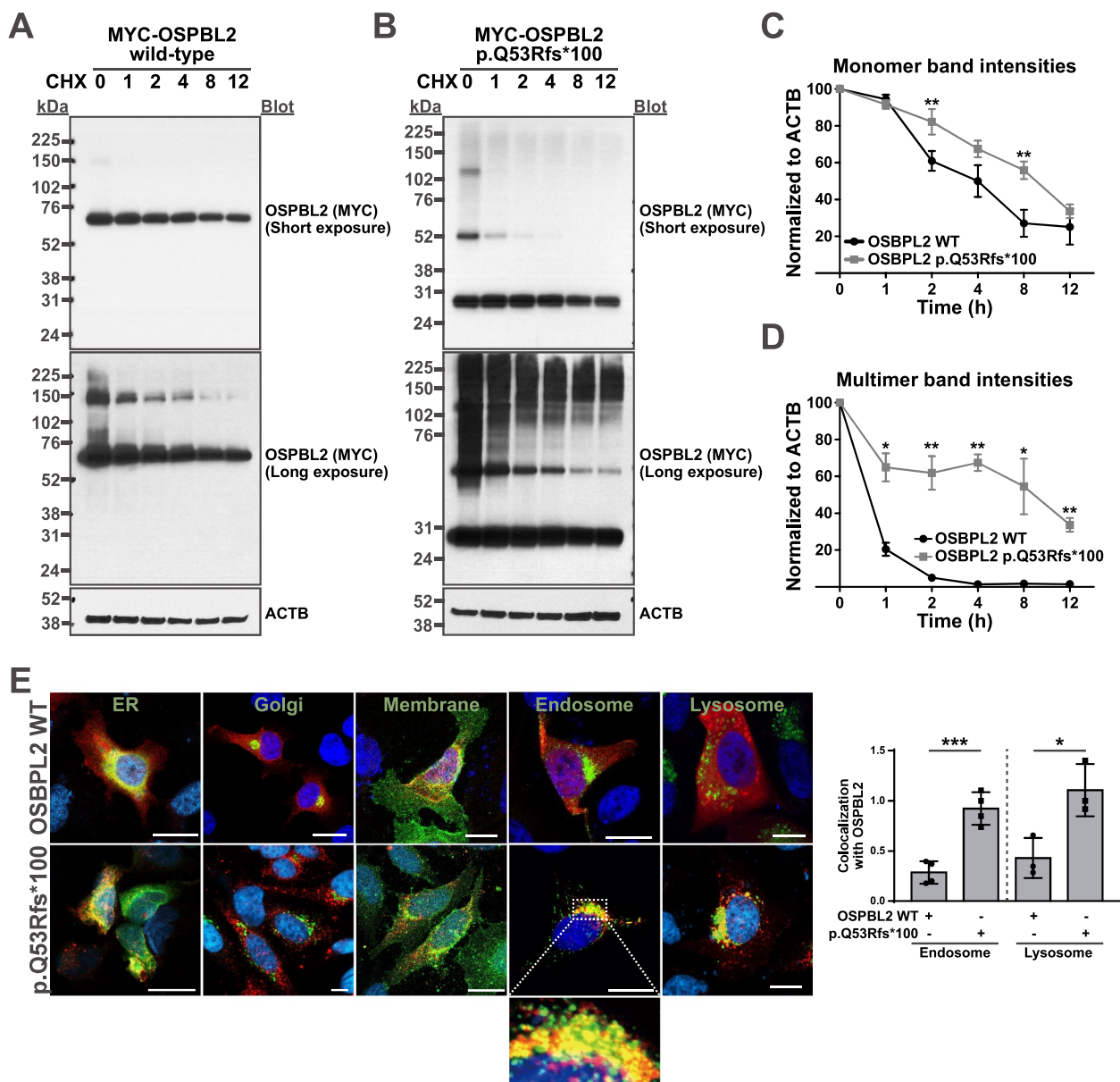


Figure 2. Effects of frameshift variants of *OSBP2* on expression. (A–D) The stability of wild-type (WT) and mutant *OSBP2* was examined using protein stability assays. Samples were harvested at the indicated times after treatment with cycloheximide (100 $\mu\text{g}/\text{ml}$). p.Q53Rfs*100 mutant, especially multimer, is more stable than *OSBP2* WT upon overexpression. Data are representative of at least three independent experiments, and band intensities were normalized to ACTB. Representative immunoblots are shown in A and B. * $p < 0.05$, ** $p < 0.01$, ANOVA with Bonferroni comparisons. (E) Immunofluorescence of *OSBP2* WT and mutant proteins in HeLa cells. Endoplasmic reticulum (ER, YFP-ER), Golgi (YFP-Golgi), membrane (GFP-Membrane), endosome (GFP-RAB5), and lysosome (GFP-LAMP1) are labeled. Colocalization was quantified by calculating Manders' colocalization coefficients. Scale bars: 20 μm . Data represent mean \pm SD. * $p < 0.05$, *** $p < 0.005$, ANOVA with Bonferroni comparisons.

OSBP2. When the two AA bases at positions 158 and 159 of *Osbpl2* cDNA were deleted to mimic the human c.158_159AAdel (p.Q53Rfs*100) mutation, the resulting protein (p.Q53Rfs*46) was shortened to 43 amino acids (Fig. S7A). In addition, mouse p.Q53Rfs*46 *OSBP2* did not form cytoplasmic aggregates or multimers (Fig. S7B–C). Therefore, we generated a transgenic mouse model that expressed an N-terminally FLAG-tagged p.Q53Rfs*100 *OSBP2* mutant (Figure 6A, designated as HsQ53R-TG). The transgene was confirmed via genotyping (Fig. S8A) and was highly expressed in the inner ear and brain (Figure 6B). HsQ53R-TG mice were viable, fertile, and born at an expected Mendelian ratio, and

did not exhibit any gross abnormalities. In addition, on P14, no obvious defects were observed in the organization and morphology of the cochlea in the organ of Corti of HsQ53R-TG mice (Fig. S8B). However, unlike *osbpl2*^{-/-} mice, HsQ53R-TG mice displayed significantly higher ABR and DPOAE thresholds at all frequencies than their control siblings on P60 (Figure 6C–D). In the whole-mount immunofluorescence of the cochlea, the transgene expression was observed in auditory hair cells and SGNs, and phalloidin staining revealed the degeneration of hair cells in HsQ53R-TG (Figure 6E). Immunofluorescence and histology also showed that hair cells were severely degenerated in the organ of Corti and SGNs were

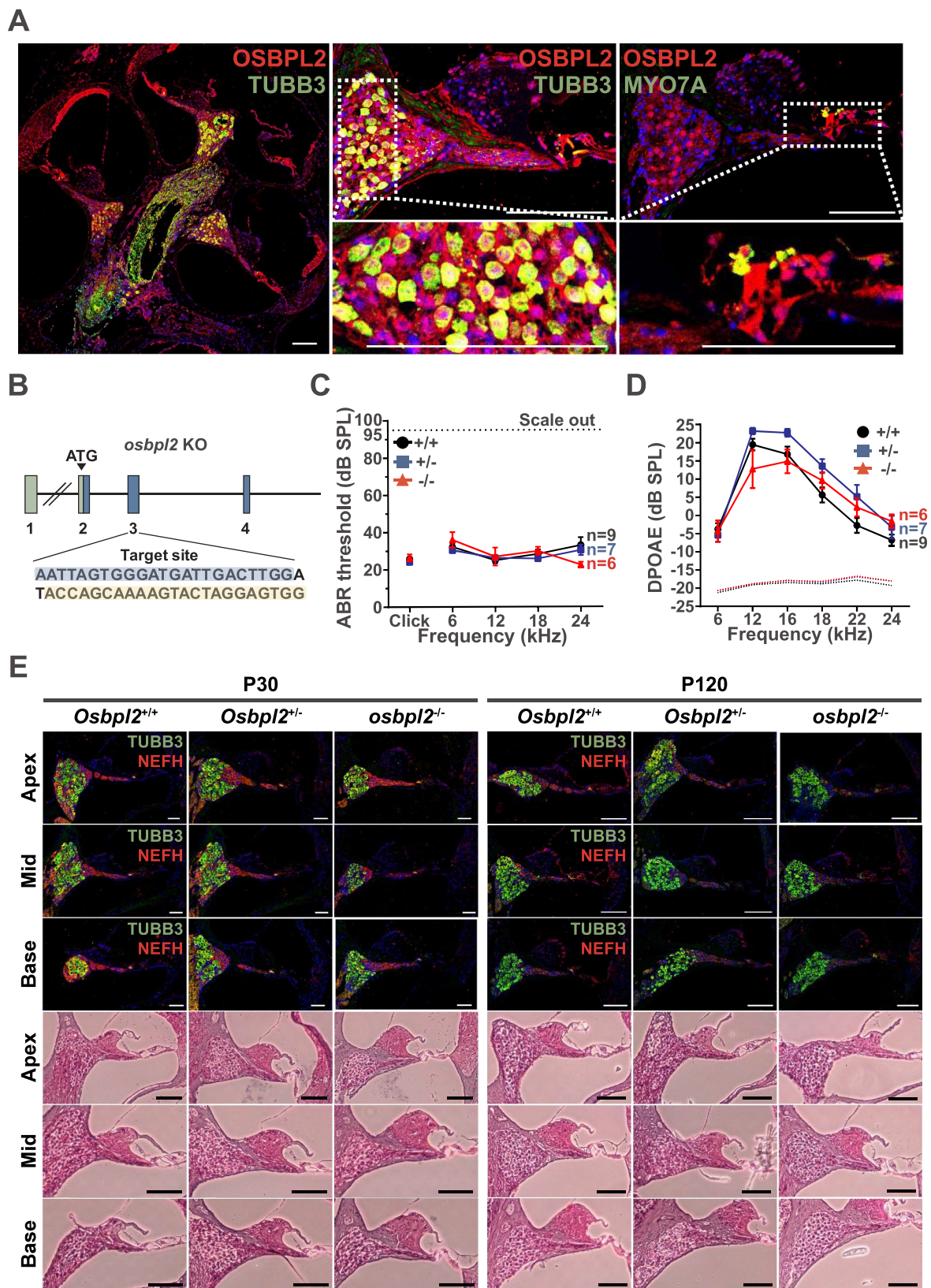


Figure 3. *Osbp12* knockout mice do not develop hearing loss. (A) Expression of OSBPL2 in the mouse cochlear. OSBPL2 (red) was co-immunostained with TUBB3 or MYO7A (green). Scale bars: 20 μ m. (B) Generation of *osbp12* knockout (KO) mice. Single-guide RNA was selected to target the exon 3 of *Osbp12*. (C-D) ABR and DPOAE thresholds in *Osbp12*^{+/+} (black), *Osbp12*^{+/-} (blue), and *osbp12*^{-/-} (red) mice on postnatal (P) day 120. Genotypes showed no significant difference in hearing function. Data represent mean \pm SD. (E) Immunohistochemistry and histology of the organ of Corti in *Osbp12* mice on P30 and P120. Anti-TUBB3 (green), anti-NEFH (red), and H&E staining show that spiral ganglion neurons of *Osbp12*^{+/+} and *osbp12*^{-/-} mice are comparable to those of *Osbp12*^{+/+} mice. In addition, hair cells are well preserved in *Osbp12*^{+/-} and *osbp12*^{-/-} mice.

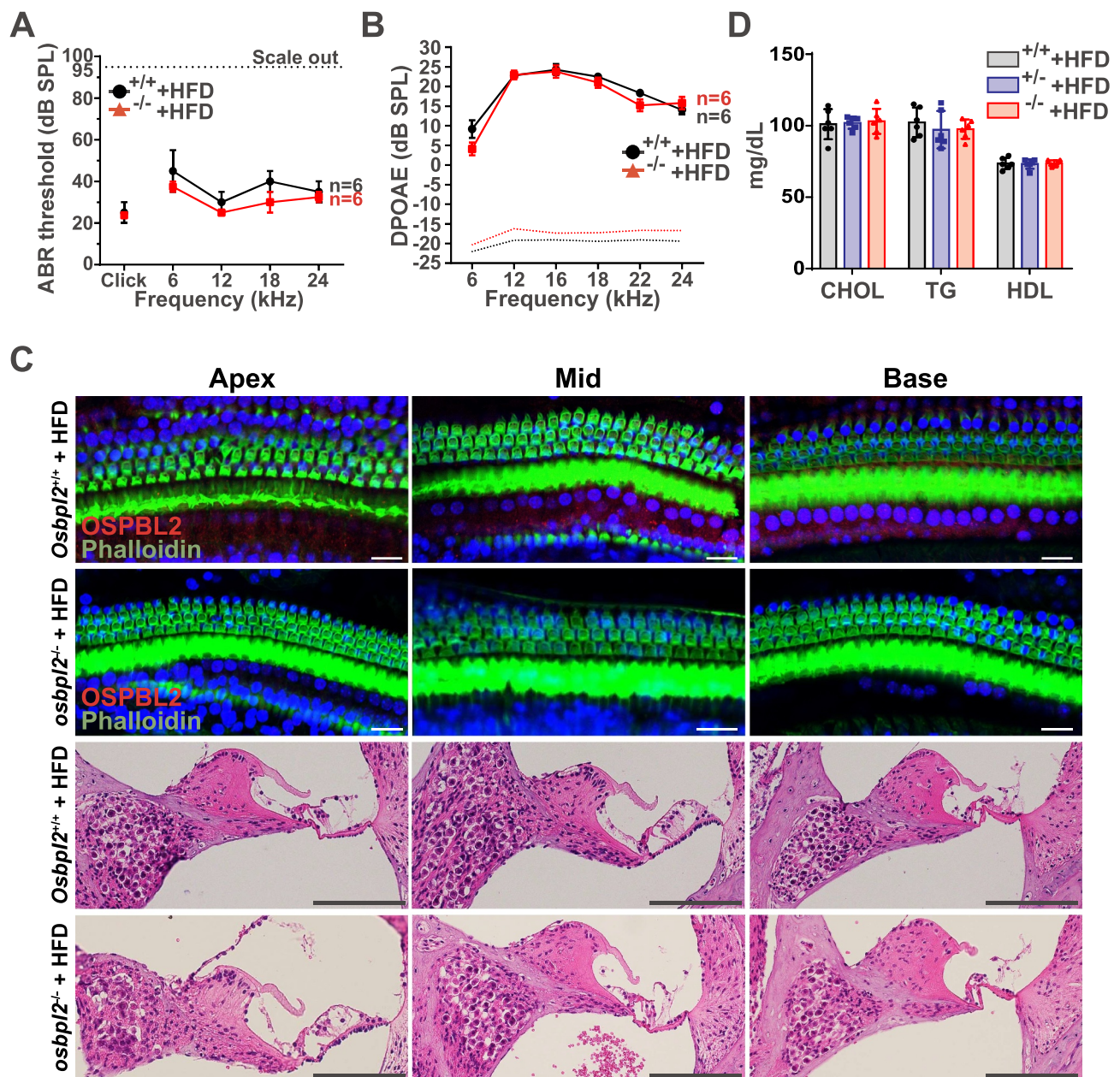


Figure 4. High-fat diet does not induce hearing loss in *osbp2* knockout mice. (A–B) ABR and DPOAE thresholds in *Osbp2*^{+/+} (black) and *osbp2*^{-/-} (red) mice fed a high-fat diet (HFD) on postnatal (P) day 120. Data represent mean \pm SD. (C) Immunostaining and H&E staining in the cochlear of *Osbp2*^{+/+} and *osbp2*^{-/-} mice that were fed HFD on postnatal P120. No significant morphological difference in inner hair cells (IHCs), outer hair cells (OHCs), and spiral ganglion neurons is shown between *Osbp2*^{+/+} and *osbp2*^{-/-} mice. White scale bars: 20 μ m; black scale bars: 100 μ m. (D) Serum cholesterol (CHOL), triglycerides (TG), and high-density lipoprotein (HDL) levels in *Osbp2*^{+/+}, *Osbp2*^{+/-}, and *osbp2*^{-/-} mice that were fed HFD for two months.

significantly reduced in HsQ53R-TG mice (Figure 6F and Fig. S8C). Cholesterol and triglyceride levels in the inner ear and brain of HsQ53R-TG mice were not different from those of control mice (Figure 6G–K), suggesting that hearing loss of HsQ53R-TG mice did not result from abnormal lipid levels. According to the novel object preference test on P60, which examines learning and memory, there was no difference between HsQ53R-TG and control mice, even though p.Q53Rfs*100 OSBPL2 diffusely accumulated in the brain tissue of HsQ53R-TG mice, suggesting that hearing loss is probably not due to defects in brain function (Figure 7A–C). In addition, we generated a transgenic mouse model, which expressed an N-terminally FLAG-tagged wild-type OSBPL2 (Figure 8A–

C, designated as HsWT-TG). However, unlike HsQ53R-TG mice, HsWT-TG mice did not develop hearing loss up to P90 (Figure 8D–F). These results suggested that transgenic expression of p.Q53Rfs*100 OSBPL2 mutant protein abrogated hearing function via cochlear degeneration.

Truncated OSBPL2 mutant leads to defective endolysosomal homeostasis and impaired autophagy

As four pathogenic OSBPL2 mutations led to almost identical truncated proteins, which formed cytoplasmic aggregates (Figure 1H and Fig. S3A), we performed a proteomic analysis

to understand the function of mutant OSBPL2 via the identification of its interactome (Fig. S9A-C). We transiently transfected HEK 293 cells with N-terminally FLAG-tagged WT and p.Q53Rfs*100 OSBPL2. Following affinity purification using anti-FLAG beads, protein eluates were analyzed using liquid chromatography coupled with a high-resolution mass spectrometer (LC-MS/MS). In total, 152 and 407 proteins were identified as exclusive interactors of WT or mutant OSBPL2, respectively. Among them, VAPB and SNRPF, which are interactors of WT OSBPL2 reported in the Human Reference Interactome (<http://www.interactome-atlas.org/>), were isolated (Figure 9A). Interestingly, SQSTM1/p62, an autophagy receptor and autophagosome cargo protein [26], was also identified as an interactor of both WT and mutant OSBPL2 (Figure 9A). We confirmed this interaction using coimmunoprecipitation and found that the interaction between p.Q53Rfs*100 OSBPL2 and SQSTM1 was very weak compared to that between WT OSBPL2 and SQSTM1 (Fig. S10A). SQSTM1 interacted with WT OSBPL2 through its region containing ZZ domain, LIR motif, or both (Fig. S10B). Gene ontology (GO) analysis showed that proteins that exclusively interacted with p.Q53Rfs*100 were

involved in protein stabilization, macroautophagy, endosome organization, regulation of MTORC1 signaling, and ubiquitination (Figure 9B and Fig. S11A-B).

As p.Q53Rfs*100 interacted with proteins related to endosomes and autophagy, we first examined the effect of WT and mutant OSBPL2 on autophagic flux via measuring total LC3 levels and LC3-II:LC3-I ratio. Overexpression of p.Q53Rfs*100 OSBPL2 decreased the ratio of active membrane-bound LC3-II to cytosolic LC3-I (Figure 9C). This was also confirmed in the inner ear tissues, but not in the brain tissues, of HsQ53R-TG mice on P60 (Figure 9D-G).

Overexpression of p.Q53Rfs*100 OSBPL2 also increased the LysoTracker signal, an acidotropic dye (Figure 10A) and decreased the degradation of ectopically introduced dextran (Figure 10B). However, the activity and expression of CTSD (cathepsin D), a lysosomal aspartyl protease, were not altered by p.Q53Rfs*100 OSBPL2 (Figure 10C-D), suggesting that the decrease in lysosomal degradative capacity in cells with mutant OSBPL2 is not due to impaired lysosomal activity, but related to impaired autophagic flux. In addition, filipin staining showed that intracellular distribution of cholesterol was not altered by the overexpression of p.Q53Rfs*100 OSBPL2 (Figure 10E), indicating

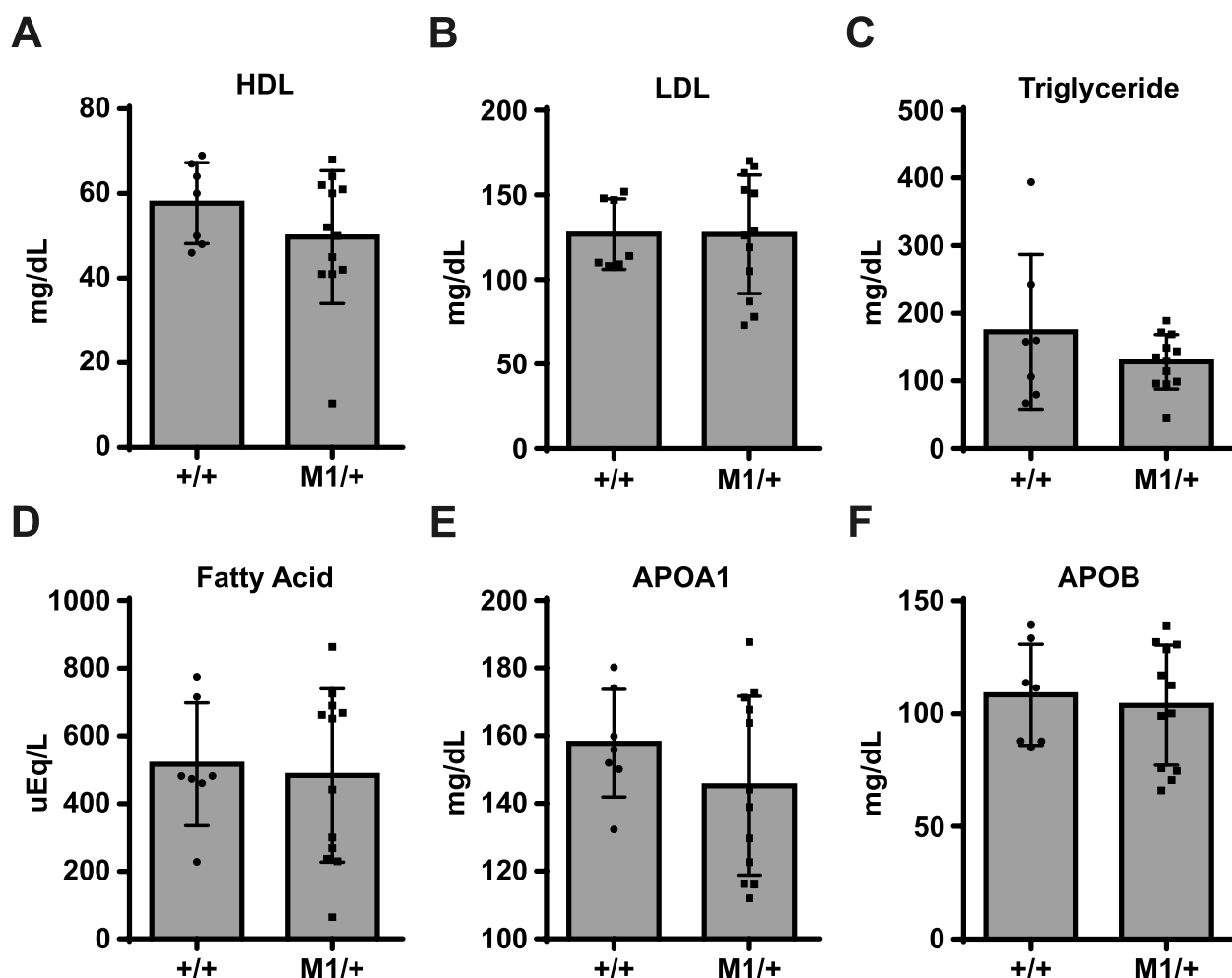


Figure 5. Serum lipid profiles of individuals with an *OSBPL2* mutation. (A-F) High-density lipoprotein (HDL), low-density lipoprotein (LDL), triglyceride, fatty acid, APOA1 (apolipoprotein A1), and APOB (apolipoprotein B) levels are not different between control individuals and individuals with an *OSBPL2* mutation. All individuals are from YUHL3 families. M1, c.158_159AAdel (p.Gln53Argfs*100).

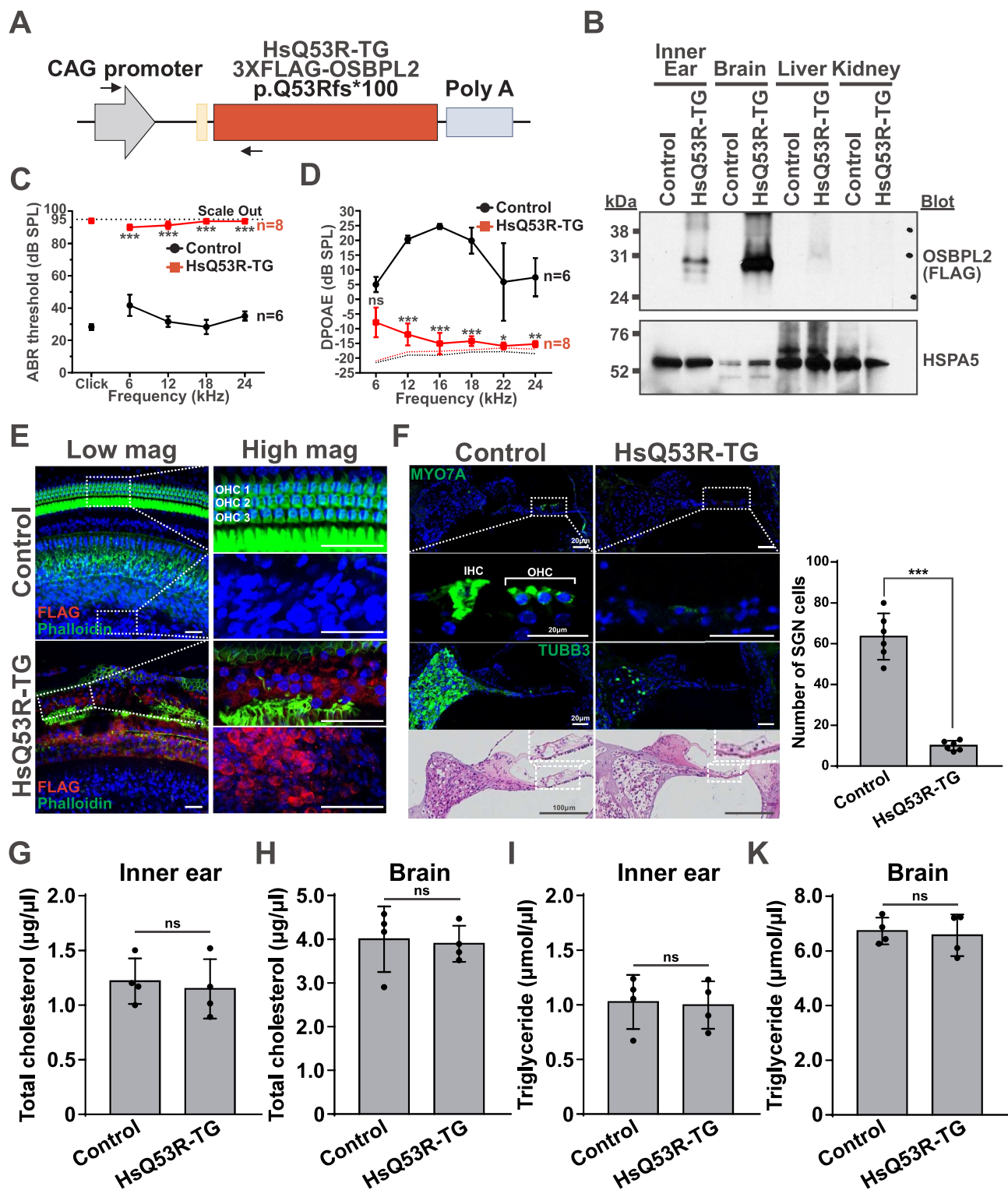


Figure 6. Transgenic mice expressing mutant OSBPL2 recapitulate hearing loss. (A) Generation of transgenic mice expressing human p.Q53Rfs*100 OSBPL2 (HsQ53R-TG). Transgene cassette consists of the CAG promoter, 3XFLAG-tagged p.Q53Rfs*100 OSBPL2, and SV40 poly(A) tail sequence; arrows indicate PCR primers for genotyping. (B) Immunoblotting of p.Q53Rfs*100 OSBPL2 in the inner ear, brain, liver, and kidney of HsQ53R-TG mice using anti-FLAG antibody. (C-D) ABR and DPOAE thresholds in control (black) and HsQ53R-TG (red) mice at P60. Compared to control mice, HsQ53R-TG mice exhibited severe hearing loss at all frequencies. Data represent the mean \pm SD. * $p < 0.05$, ** $p < 0.01$, *** $p < 0.005$, ns not significant, ANOVA with Bonferroni comparisons. (E) Immunostaining with phalloidin (green) and FLAG (red) of the whole-mount inner ear showed severe degeneration in the organ of Corti and mutant protein aggregation in the spiral ganglion of HsQ53R-TG mice on P60. Scale bars: 100 μ m. (F) Immunohistochemistry and histology of the organ of Corti of HsQ53R-TG mice on P60. Anti-TUBB3, anti-MYO7A, and H&E staining show spiral ganglion neurons (SGNs) and hair cell degeneration in HsQ53R-TG mice. Graph represents the mean \pm SD of the number of SGN cells. *** $p < 0.005$, Student's *t*-test. (G-K) Total cholesterol (G-H) and triglyceride (I-K) levels in inner ear and brain were not different between control and HsQ53R-TG mice. Data represent mean \pm SD. ns not significant; Student's *t*-test.

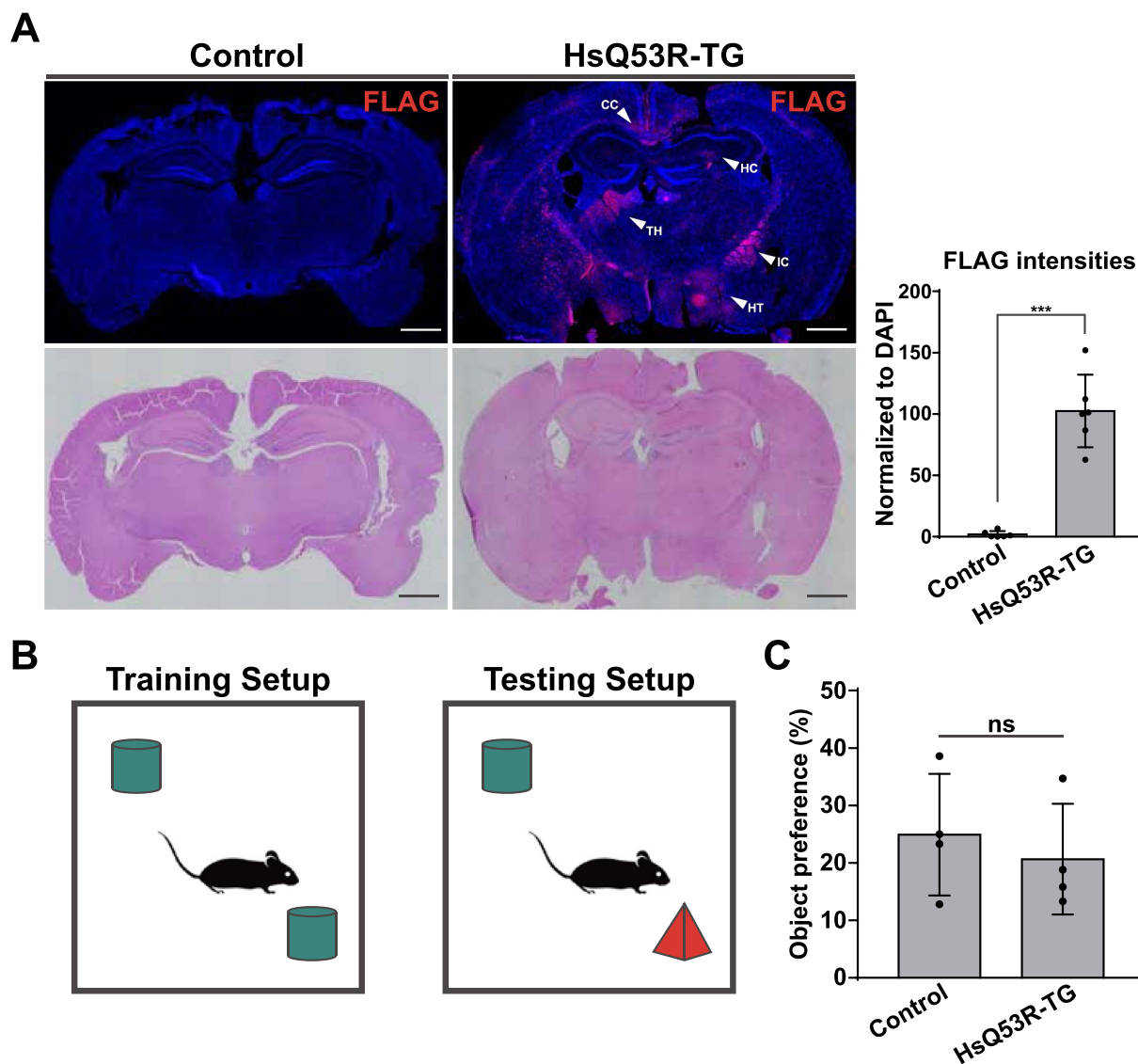


Figure 7. Mutant OSBPL2 protein in the brain and behavior test of HsQ53R-TG mice. (A) Immunostaining with an anti-FLAG antibody showed mutant OSBPL2 accumulates aggregation in the brain of HsQ53R-TG mice on P60. Histology showed no gross abnormality in HsQ53R-TG mice. Graph represents the mean \pm SD of fluorescence intensity. *** $p < 0.005$, Student's t-test. CC, corpus callosum; HC, hippocampus; HT, hypothalamus; IC, Internal capsule; TH, thalamus. Scale bars: 1 mm. (B-C) Novel object recognition. Both control and HsQ53R-TG mice showed no difference in preference for the novel object. Data represent mean \pm SD. ns not significant; Student's t-test.

that perturbed endolysosomal homeostasis resulting from mutant OSBPL2 was not attributable to improper cholesterol localization.

Immunoprecipitation of OSBPL2 proteins showed that levels of high molecular weight polyubiquitinated proteins were increased in cells overexpressing p.Q53Rfs*100 OSBPL2 compared to cells overexpressing WT OSBPL2 (Figure 11A). Interestingly, rapamycin treatment decreased both polyubiquitinated protein levels and multimer-size bands of p.Q53Rfs*100 (Figure 11A). Overexpression of WT OSBPL2 decreased PIK3CA, AKT, and MTOR phosphorylation, whereas p.Q53Rfs*100 OSBPL2 overexpression resulted in increased MTOR phosphorylation (Figure 11B). Enhanced MTOR phosphorylation caused by p.Q53Rfs*100 OSBPL2 was also decreased upon rapamycin treatment (Figure 11B). Overexpression of p.Q53Rfs*100 OSBPL2 did not change the expression of proteins related to unfolded protein response, such as ERN1/IRE1 α ,

HSPA5/BiP, and XBP1 (Fig. S12). p.Q53Rfs*100 OSBPL2 partially colocalized with LC3 and SQSTM1, which was enhanced upon rapamycin treatment (Figure 11C-F).

Rapamycin partially rescued the hearing loss phenotype in HsQ53R-TG mice and individuals with DFNA67

As rapamycin decreased multimer bands of p.Q53Rfs*100 *in vitro*, we further investigated whether rapamycin could rescue the hearing loss in HsQ53R-TG mice. Because hearing impairment of HsQ53R-TG mice was detected as early as P21, we administered rapamycin starting from P1 daily (Figure 12A, Strategy #1), but the injection was stopped on P10 due to growth retardation (Fig. S13A-B). Rapamycin was given daily for a month starting on P30, but it did not show efficacy when the hearing was measured on P60 (Figure 12A, Strategy #3, and Fig.

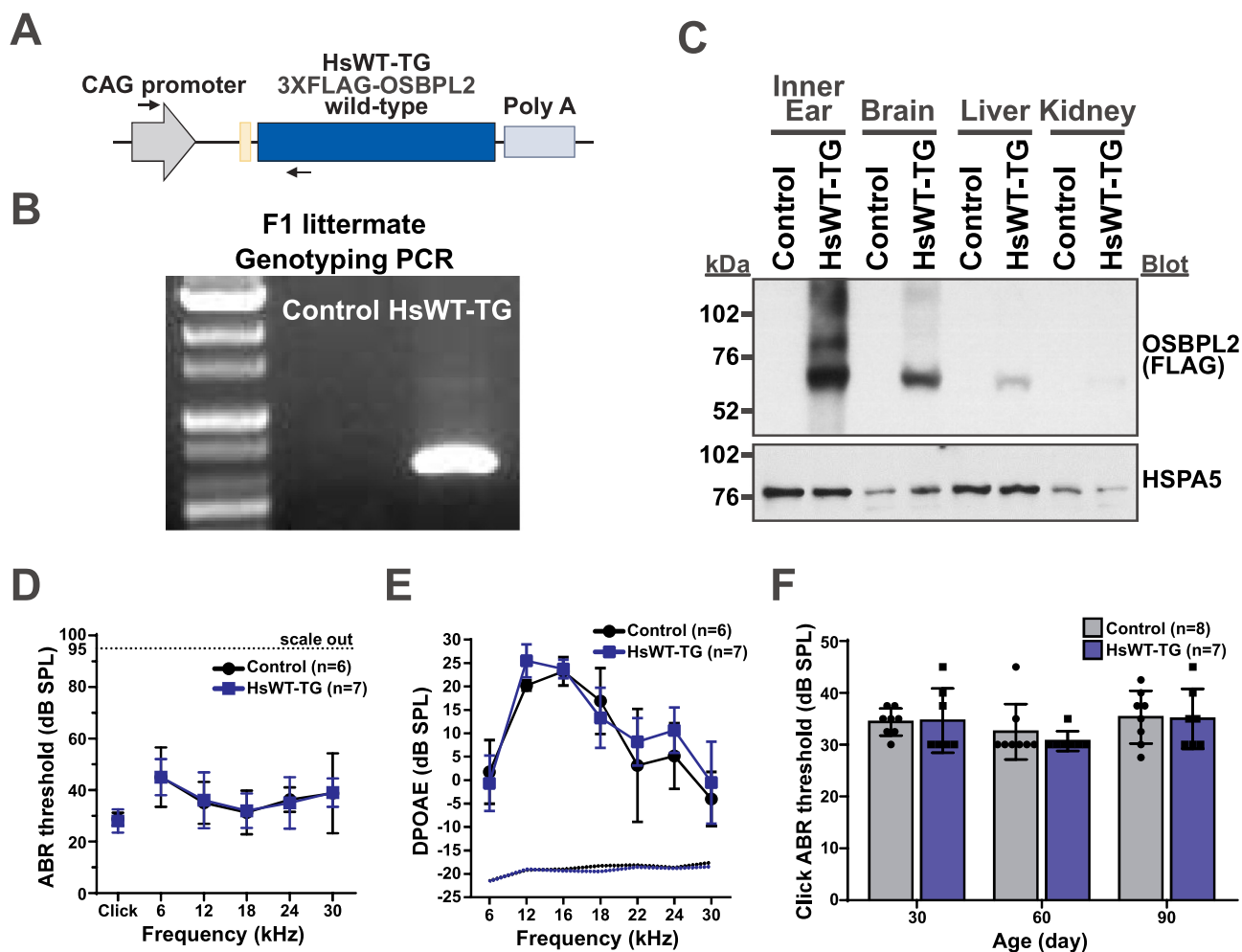


Figure 8. Transgenic mice expressing wild-type OSBPL2 do not show hearing loss. (A) Generation of transgenic mice expressing human wild-type OSBPL2 (HsWT-TG). Transgene cassette consists of the CAG promoter, 3XFLAG-tagged WT OSBPL2, and SV40 poly(A) tail sequence; arrows indicate PCR primers for genotyping. (B) PCR genotyping of HsWT-TG mice. The forward primer is for the CAG promoter region, and the reverse primer is for the coding region of *OSBPL2* cDNA. The amplicon size is 643 bp. (C) Immunoblotting of WT OSBPL2 in the inner ear, brain, liver, and kidney of HsWT-TG mice using anti-FLAG antibody. (D-E) ABR and DPOAE thresholds in control (black) and HsWT-TG (blue) mice at P60. Data represent mean \pm SD. (F) Click ABR thresholds of control and HsWT-TG mice up to 90 postnatal days.

S13C). Therefore, we injected rapamycin daily from P7 to P15 and measured the hearing sensitivity on P30 (Figure 12A, Strategy #2). Interestingly, rapamycin treatment significantly decreased both ABR and DPOAE thresholds, especially at low frequencies in HsQ53R-TG mice (Figure 12B-D). Histology and immunofluorescence showed that hair cells and SGNs were preserved in HsQ53R-TG mice upon rapamycin treatment compared to mice without treatment (Figure 12E and Fig. S13D). In addition, p.Q53Rfs*100 OSBPL2 expression, detected using anti-FLAG antibody in SGNs of HsQ53R-TG mice, was significantly decreased upon rapamycin treatment (Figure 12E). SEM of cochlear on P60 showed that stereocilia were abrogated in HsQ53R-TG mice compared to control mice but were partially rescued upon rapamycin treatment in HsQ53R-TG mice (Figure 12F). Transmission electron microscopy (TEM) revealed large electron-dense structures in the cytoplasm of type 1 SGNs, which resembled insoluble protein deposits, but rapamycin treatment significantly decreased these structures in HsQ53R-TG mice (Figure 12G).

Based on our findings, we performed a proof-of-concept clinical trial, in which individuals with *OSBPL2* mutations

from the YUHL3 and YUHL457 families were treated with rapamycin (Rapamune, Pfizer). Five enrolled adult patients with mild to severe hearing loss received 2 mg of rapamycin once a day for 3 months (Figure 13A). We compared the hearing thresholds at low frequencies including 250 and 500 Hz before and after rapamycin treatment (Figure 13B-C); while the hearing threshold at 250 Hz did not change at 3 and 6 months after the treatment, the hearing threshold at 500 Hz improved by \sim 5 dB. In one patient, who initially showed a response upon DPOAE (YUHL457: IV-2) (Figure 13D-E), the signal-to-noise ratio was increased bilaterally (Figure 13F). Tinnitus was identified in two patients; the symptom improved according to the Tinnitus Handicap Inventory (THI) questionnaire (Figure 13G) [27–36]. No critical side effects or other safety issues were observed in these patients after 3 months of treatment.

Taken together, these findings demonstrated that defective autophagy contributed to the pathogenesis of hearing loss in HsQ53R-TG mice and supported the therapeutic potential of rapamycin for the treatment of hearing loss resulting from the accumulation of mutant OSBPL2.

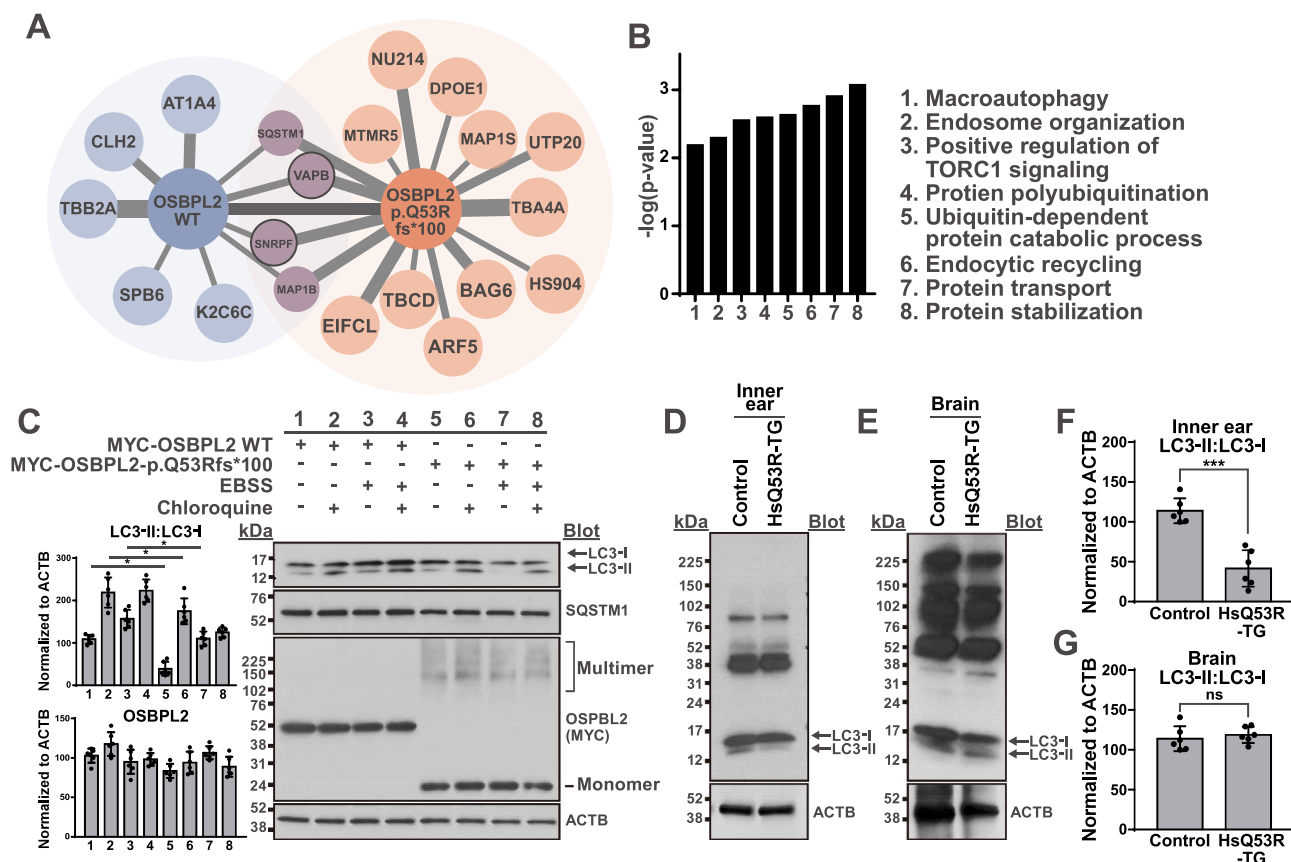


Figure 9. Mutant OSBPL2 causes autophagic impairment. (A) Representative interactors of wild-type (WT) and p.Q53Rfs*100 OSBPL2 identified using proteomics. Proteins in purple were commonly detected in both WT and mutant OSBPL2. Proteins in blue were identified as interactors of WT OSBPL2, whereas proteins in red were bound to mutant OSBPL2. SNRPF and VAPB (shown in purple with black borderline) are the known interactors of WT OSBPL2. (B) Gene ontology analysis of mutant OSBPL2 interactors revealed that proteins involved in ubiquitination and autophagy were enriched. (C) Autophagic flux assay revealed that LC3-I to LC3-II conversion was decreased in cells overexpressing p.Q53Rfs*100 OSBPL2. Forty-eight h after transfection, cells were serum-starved in Earle's balanced salt solution (EBSS) and/or treated with 10 μ M chloroquine for 4 h to induce or inhibit autophagy, respectively. * $p < 0.05$, ANOVA with Bonferroni comparisons. (D-G) Immunoblotting of LC3 in the inner ear and brain tissues of control and HsQ53R-TG mice. The ratio of LC3-II to LC3-I was decreased in the inner ear tissues (D, F) of HsQ53R-TG mice on P60, but not in brain tissues (E, G). Graph represents the mean \pm SD of band intensity. *** $p < 0.005$, ns: non-significant, Student's t-test.

Discussion

In this study, we elucidated the molecular mechanisms underlying autosomal dominant NSHL, DFNA67, resulting from truncating *OSBPL2* mutations, and showed that it is a toxic proteinopathy. Using cell and transgenic mouse models, we showed that truncated mutant OSBPL2 accumulated intracellularly, thereby impairing autophagic function, leading to hearing loss in HsQ53R-TG mice. We also demonstrated that rapamycin, an inducer of autophagy, decreased the accumulation of the mutant protein and partially rescued the hearing loss phenotype in HsQ53R-TG mice. This study has important implications for the prevention and treatment of DFNA67.

Including the results of this study, four frameshift and one missense mutations in *OSBPL2* have been reported to cause DFNA67 [7–9]. Four frameshift mutations resulted in truncated proteins which contained 49–59 N-terminal amino acids of WT OSBPL2 and the frameshifted, 92–102 amino acid-long peptides, therefore; the resulting proteins were all 151 amino acids in length. In addition, the added frameshifted peptides did not match any of the human proteins in the BLASTP search; therefore, they were so-called neo-proteins. We found

that these mutant proteins formed intracellular aggregates, whereas the only reported missense variant, p.L195M, did not, suggesting that the pathogenicity of the p.L195M variant needs to be reevaluated. We also demonstrated that HsQ53R-TG mice exhibited progressive hearing loss and the transgene, p.Q53Rfs*100 OSBPL2, accumulated in the organ of Corti and SGNs of HsQ53R-TG mice. Taken together, DFNA67 resulted from the accumulation of neo-proteins which do not normally exist; therefore, we identified DFNA67 as a proteinopathy.

Our study also explained the autosomal dominant inheritance of DFNA67. *OSBPL2* had a pLI (probability of being loss-of-function intolerant) score of 0.13 and an observed/expected ratio of 0.26; suggesting that haploinsufficiency was not likely to occur. This was consistent with our finding that *Osbp2*^{+/-} mice did not develop hearing loss. Nineteen loss-of-function alleles of *OSBPL2* were reported in the gnomAD, none of them presented a neo-protein like p.Q53Rfs*100, and no homozygous individual for these alleles existed. Comparison of *osbp2*^{-/-} and HsQ53R-TG mice indicated that hearing loss was not due to loss-of-function of OSBPL2, but to the abnormal function of OSBPL2 mutant neo-protein. In this regard, it is contradictory that *OSBPL2*^{-/-} pigs exhibit hearing loss [14], whereas *osbp2*^{-/-} mice do not. Yao et al.

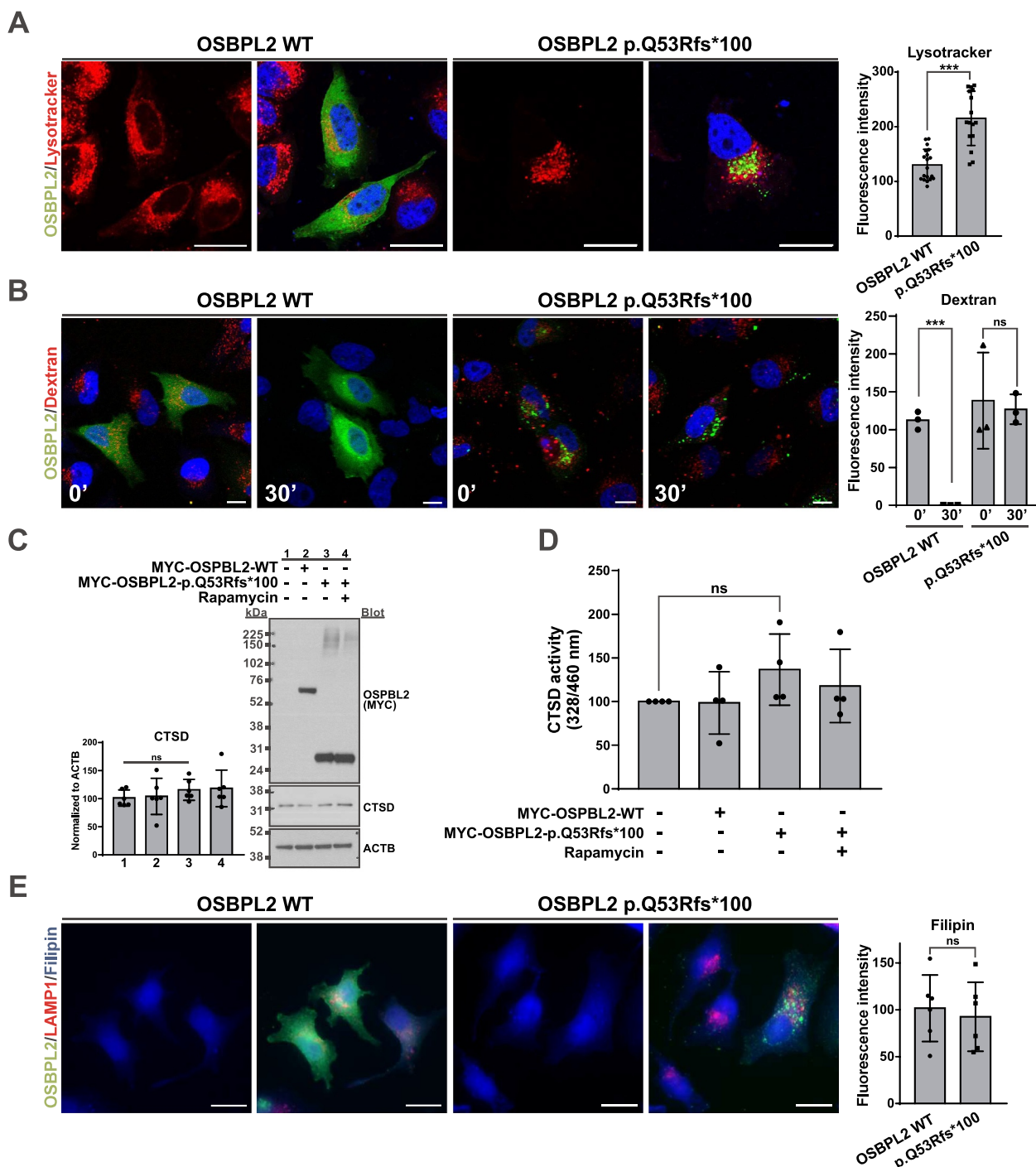


Figure 10. Mutant OSBPL2 causes perturbed endolysosomal homeostasis. (A) The signal intensity of LysoTracker was increased in cells overexpressing p.Q53Rfs*100 OSBPL2 compared to cells overexpressing WT OSBPL2. HeLa cells transfected with indicated plasmids were incubated with 200 nM LysoTracker for 1 h at 37°C. Scale bars: 20 μ m. *** $p < 0.005$; Student's t-test. (B) Rhodamine-labeled dextran was more accumulated in cells overexpressing p.Q53Rfs*100 OSBPL2 compared to cells overexpressing WT OSBPL2. Scale bars: 20 μ m. *** $p < 0.005$, ANOVA with Bonferroni comparisons. (C) Overexpression of p.Q53Rfs*100 OSBPL2 did not affect the level of CTSD. (D) The enzyme activity of CTSD was not affected by overexpression of p.Q53Rfs*100 OSBPL2. Data represent the mean \pm SD. (E) Filipin staining (blue) revealed that intracellular cholesterol distribution was not defective in cells overexpressing p.Q53Rfs*100 OSBPL2. Scale bars: 20 μ m.

obtained three OSBPL2-disrupted alleles, p.T96Hfs*230, p.E97_M99del, and p.Y98Lfs*231 using the CRISPR-Cas9 system and mostly used p.Y98Lfs*231-homozygous pigs for their experiments. It would be interesting to examine whether p.Y98Lfs*231 behaves like p.Q53Rfs*100 and whether p.Y98Lfs*231-heterozygous pigs exhibit hearing loss.

More importantly, we found that accumulated OSBPL2 mutant neo-proteins perturbed endolysosomal homeostasis

associated with impaired autophagy, an evolutionarily conserved lysosomal degradation process indispensable for cell homeostasis. Unlike WT OSBPL2, p.Q53Rfs*100 neo-protein had interactors involved in macroautophagy, regulation of MTORC1 signaling, and ubiquitination. Neo-proteins formed multimers even in a denaturing condition, increased the level of high molecular weight polyubiquitinated proteins, and decreased autophagic flux. HsQ53R-TG mice, which

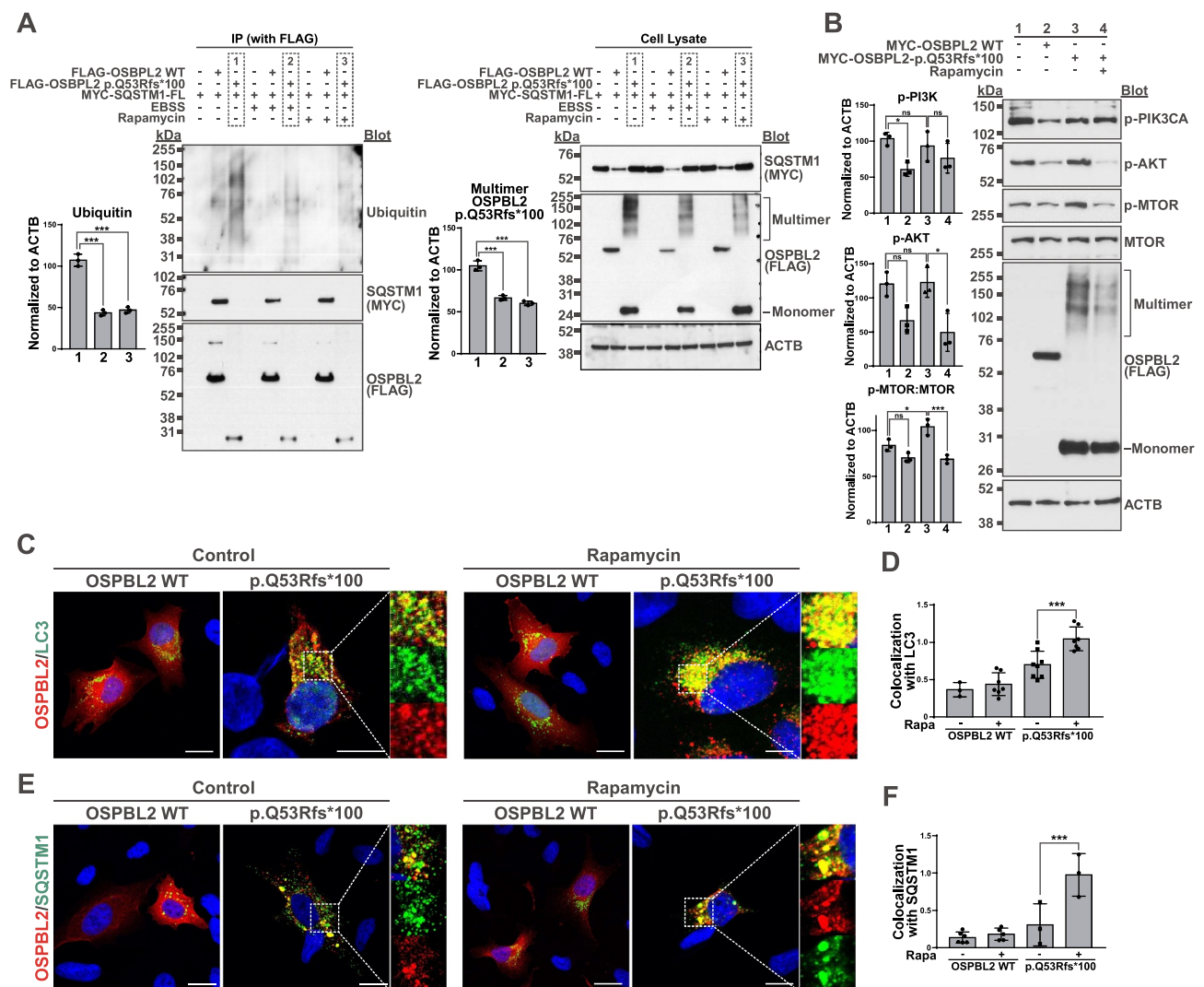


Figure 11. Rapamycin rescues cellular defects resulting from mutant OSBPL2. (A) Overexpression of p.Q53Rfs*100 OSBPL2 increased high molecular weight polyubiquitinated proteins, whereas 3 μ M rapamycin treatment or nutrient starvation reduced mutant OSBPL2 multimers as well as polyubiquitinated proteins. HEK 293 cells were transfected as indicated and harvested. Protein samples were immunoprecipitated with anti-FLAG antibody and immunoblotted using anti-ubiquitin, anti-MYC, and anti-FLAG antibodies. FL, full-length. *** $p < 0.005$, ANOVA with Bonferroni comparisons. (B) Overexpression of p.Q53Rfs*100 OSBPL2 induced MTOR phosphorylation, whereas that of WT OSBPL2 did not. MTOR phosphorylation caused by the overexpression of mutant OSBPL2 was decreased upon 3 μ M rapamycin treatment. Densitometry analyses in (A–B) are representative of at least three independent experiments and band intensities were normalized to that of ACTB. * $p < 0.05$, *** $p < 0.005$, ns non-significant, ANOVA with Bonferroni comparisons. (C–F) Rapamycin treatment increased colocalization of autophagy markers, LC3 and SQSTM1, with p.Q53Rfs*100 OSBPL2. mCherry-LC3 or GFP-SQSTM1 and OSBPL2 containing plasmids were transfected into HeLa cells and were subjected to 3 μ M rapamycin treatment for 24 h. Colocalization was quantified by calculating Manders' colocalization coefficients. Scale bars: 20 μ m. *** $p < 0.005$, ANOVA with Bonferroni comparisons.

expressed p.Q53Rfs*100 OSBPL2 exhibited mutant protein accumulation, together with cytoplasmic vacuolization and atypical electron-dense structures observed via electron microscopy of the inner ear. These results suggested that defective autophagy underlay the observed hearing loss phenotype. These findings are in line with emerging evidence indicating a role for protein homeostasis and autophagy in the maintenance of cochlear function [28–30]. Defective proteostasis and autophagy led to age-related hearing loss in mouse models. Our data demonstrated that defects in these processes indeed contributed to the pathogenesis of hearing loss in humans. Several genetic disorders in the autophagy pathway have been described and characterized by prominent involvement of the central nervous system, peripheral nerves, and skeletal muscles. For example, Ohtahara syndrome

(OMIM 612186) resulting from mutations in *DMXL2* commonly accompanies sensorineural hearing impairment, optic atrophy, and myopathy [31,32].

We discovered that rapamycin inhibited the accumulation of OSBPL2 neo-proteins, thereby rescuing endolysosomal function and autophagy. Furthermore, 9-day rapamycin treatment delayed the progress of hearing loss in HsQ53R-TG mice. Though the number of patients enrolled in a clinical trial was insufficient to reach out statistical significance, we observed that the enrolled patients improved the symptom of tinnitus and partially improved auditory thresholds at low frequencies. In this regard, patients with DFNA67 are an optimal candidate for medical intervention, because they show progressive hearing loss with the onset in their late 20s and maintain residual hearing for a while without congenital

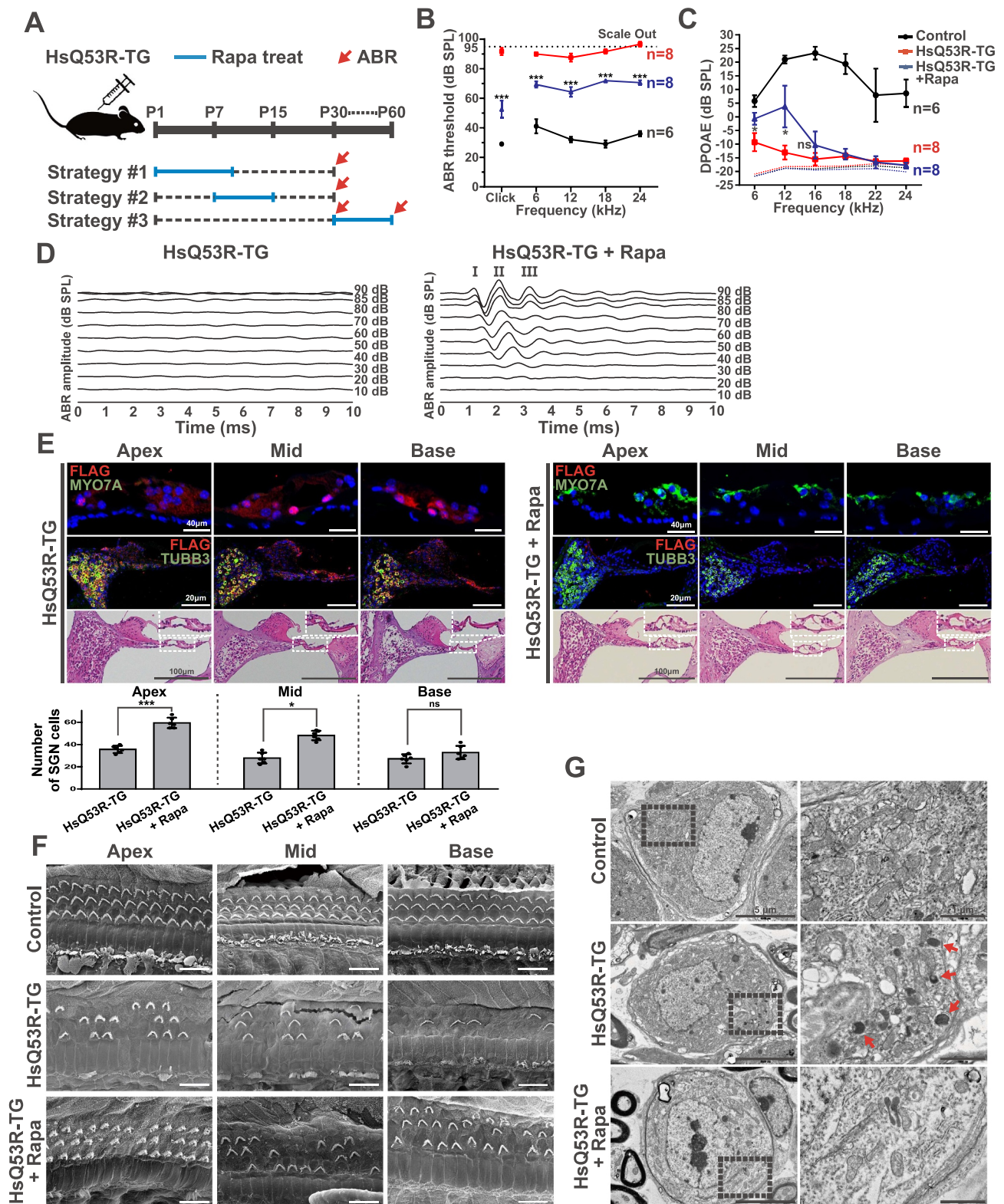


Figure 12. Rapamycin partially rescues hearing loss phenotypes of HsQ53R-TG mice. (A) Schematic diagram of strategies for rapamycin (Rapa, 2 mg/kg) treatment. Rapamycin was intraperitoneally injected daily from postnatal (P) day 1 to P10 in Strategy #1, from P7 to P15 in Strategy #2, and from P30 to P60 in Strategy #3. Hearing ability was examined on P30 and P60. Rapa, rapamycin. (B-C) ABR and DPOAE thresholds in control (black), HsQ53R-TG (red), and HsQ53R-TG mice treated with rapamycin using Strategy #2 (blue) on P60. Rapamycin treatment significantly reduced the ABR click threshold to 40 dB in HsQ53R-TG mice. DPOAE amplitudes were also restored at 6 and 12 kHz in HsQ53R-TG mice treated with rapamycin. Data represent mean \pm SD. * $p < 0.05$, *** $p < 0.005$, ns not significant, ANOVA with Bonferroni comparisons. (D) Representative ABR recordings in response to click stimuli showed sound-evoked potentials in HsQ53R-TG mice treated with rapamycin, indicating that rapamycin rescued hearing phenotype. (E) Immunohistochemistry and histology of HsQ53R-TG mice untreated or treated with rapamycin at P30. MYO7A, TUBB3, and H&E staining showed that hair cells and spiral ganglion neurons (SGNs) were more preserved in rapamycin-treated HsQ53R-TG mice compared to untreated HsQ53R-TG. Rapamycin also decreased the intensity of transgene p.Q53Rfs*100 OSBPL2, as detected using the anti-FLAG antibody. Graph represents the mean \pm SD of the number of SGN cells. * $p < 0.05$, *** $p < 0.005$, ns: non-significant, Student's t-test. (F) Scanning electron microscopy (SEM) of the inner ear of HsQ53R-TG mice treated with or without rapamycin compared to control mice. SEM images of rapamycin-treated HsQ53R-TG mice showed partial restoration of hair

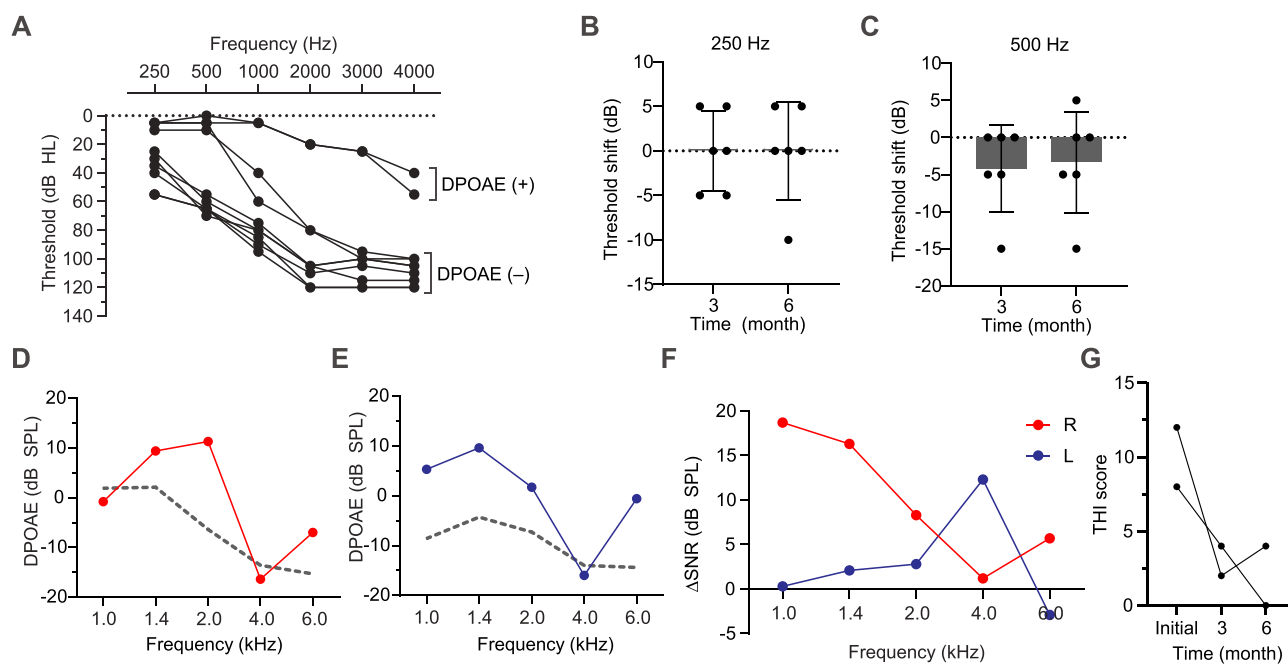


Figure 13. Effects of rapamycin on individuals with DFNA67 from YUHL3 and YUHL457 families. (A) The pure-tone audiogram of the individuals ($n = 5$) with DFNA67 from YUHL3 and YUHL457 families was obtained before the administration of rapamycin (Rapamune, Pfizer) for 3 months (2 mg, daily). Data for both ears are shown; the enrolled patients initially showed mild to severe-profound hearing loss. One patient showed positive response in DPOAE. (B-C). Three and six months later, the change in the auditory threshold was calculated from pure-tone audiogram; while the auditory threshold at 250 Hz did not change, it improved at 500 Hz in 3 out of 6 patients. (D-F) Distortion product otoacoustic emission (DPOAE) thresholds were obtained in a patient who only had an initial response (YUHL457: IV-2). Both ears [right, red in (D); left, blue in (E)] showed positive responses in DPOAE at all frequencies except at 4 kHz. Dash line indicates the background noise level. Changes in the signal-to-noise ratio (SNR) were positive in both ears after 3 months of rapamycin treatment (F). (G) Tinnitus handicap inventory (THI) score was evaluated in two patients who had tinnitus symptom before the rapamycin treatment. Three and six months later, THI score was improved.

anomalies. As such, they can have a relatively long therapeutic time window for the intervention, which give them many opportunities to remedy the hearing loss. However, there is a limitation of hearing restoration at high frequencies, of which the hearing function was too devastated to recover; it implies that the optimization of therapeutic time window is important for the efficient intervention.

In conclusion, we elucidated the molecular mechanism underlying DFNA67, a proteinopathy caused by mutant *OSBPL2* protein which is associated with lysosomal defects and impaired autophagy, and suggested rapamycin as a therapeutic candidate for DFNA67, for which currently no medical intervention is available. More studies are required to establish a rapamycin treatment regime and identify more efficient and less toxic compounds than rapamycin to establish precision medicine in genetic hearing loss.

Materials and methods

Patients and sensorineural hearing loss diagnosis

All patients who were registered in the YUHL cohort had hearing loss and were referred to Severance Hospital for further evaluation and treatment. Pure-tone and speech audiograms were performed for all patients and their affected and unaffected

family members. Pure-tone air (250–8,000 Hz) and bone conduction (250–4,000 Hz) thresholds were measured using clinical audiometers in a double-walled audio booth. The degree of hearing loss was determined by averaging the thresholds of air conduction at 500, 1000, 2000, and 4000 Hz. The steady-state auditory response was also determined for young babies. Temporal bone computed tomogram and magnetic resonance imaging were performed to evaluate inner ear anomalies.

We performed a proof-of-concept clinical trial in which individuals with *OSBPL2* mutations from the YUHL3 family are being treated with Rapamune (Pfizer, S1039). This trial was reviewed and approved by the IRB at the Severance Hospital (#2020-0250) and the Ministry of Food and Drug Safety (#33,042). Three enrolled adult patients with residual hearing function at low frequencies took 2 mg of rapamycin daily for 3 months. The primary endpoint was assessed after Rapamune intake for 3 and 6 months to decide whether the treatment is safe and efficient in terms of improvement of the hearing threshold at low frequencies in pure-tone audiogram and decrease of tinnitus symptom in THI score.

ETHICS APPROVAL

This study was approved by the institutional review board of the Severance Hospital, Yonsei University Health System (IRB

#4-2015-0659). We obtained informed written consent from individuals with hearing loss for participation in this study and publication of their clinical data and enrolled them in the YUHL cohort.

WES

Genomic DNA was extracted from peripheral blood obtained from the affected individuals and their parents (if available), using RBC Lysis Solution (iNtRon Biotechnology, 172 R-1000), Cell Lysis Solution (iNtRon Biotechnology, 172C-1000), and Protein Precipitation Solution (iNtRon Biotechnology, 172C-0350). WES and variant filtering were performed as described previously [23], using an Agilent SureSelect V5 enrichment capture kit (Agilent Technologies, 5990-9857) and Illumina HiSeq 2500 platform (101 bases, paired-end). Sequence reads were mapped to the human reference genome assembly (NCBI build 3/hg19) using CLC Genomic Workbench (version 9.5.3) software (Qiagen). All variants with a minimum coverage of two were used. Variants were called using Basic Variant Caller in CLC Workbench and then annotated.

Reverse transcription real-time PCR

Whole-blood RNA was isolated from each patient and healthy subject, using TRIzol reagent (Thermo Fisher Scientific, 15,596,026). Exactly 1 µg of total RNA was added in a final volume of 20 µl for reverse transcription using an iScript™ Select cDNA Synthesis Kit (Bio-Rad, 1,708,896) according to the manufacturer's instructions. Real-time PCR was performed in 96-well plates using the StepOnePlus™ Real-Time PCR System and TaqMan Master Mix (Thermo Fisher Scientific, 4,369,016) according to the manufacturer's instructions. The probes used were *GAPDH* (Thermo Fisher Scientific, Hs02758991_g1) and *OSBPL2* (Thermo Fisher Scientific, Hs01023271_m1). Each PCR reaction was run in triplicate. Relative gene expression levels were calculated using the threshold cycle (Ct) method with *GAPDH* as the control: $\Delta Ct = Ct(GAPDH) - Ct(OSBPL2)$. The fold change of *OSBPL2* was normalized to that of *GAPDH*, relative to the control samples, and calculated as $2^{-\Delta\Delta Ct}$.

Plasmid construction and site-directed mutagenesis

cDNA of human *OSBPL2* was purchased from OriGene Technologies (RC201344) and subcloned into the pENTR-D-TOPO vector (Invitrogen, K240020). Expression vectors were constructed using LR clonase (Invitrogen, 11,791,019) following the manufacturer's instructions, with a MYC- or FLAG-tag at the N terminus. *OSBPL2* mutant clones were generated via PCR-based site-directed mutagenesis using the Quick Change II XL site-directed mutagenesis kit (Agilent Technologies, 200,521). In addition, *OSBPL2* cDNA was cloned into p3XFLAG-CMV™-10 (Sigma, E7658) and pCAGGS (RDB08938, Riken). SQSTM1/p62 plasmids were kindly provided by Dr Yong Tae Kwon (College of Medicine, Seoul National University). The following vectors were used: p3XFLAG-CMV™-7 (Sigma, E7408), pEYFP-Golgi

(Clontech, 6909-1), pEYFP-ER (Clontech, 6906-1), pCAG-mGFP-Membrane (Addgene, 14,757; deposited by Connie Cepko), GFP-RAB5 (Addgene, 31,733; deposited by Ron Vale), and GFP-LAMP1 (Addgene, 16,290; deposited by Ron Vale).

Cell culture and transfection

Human embryonic kidney 293 (HEK 293; Korean Cell Line Bank, 21,573) and HeLa (Korean Cell Line Bank, 10,002) cells were cultured in Dulbecco's modified essential medium (DMEM; Gibco BRL, 11,965,092) supplemented with 10% fetal bovine serum (FBS; Sigma, F2442) and penicillin (50 IU/ml)-streptomycin (50 µg/ml) (Gibco BRL, GIB-15410-122) (37°C, 5% CO₂) following standard protocols. HEI-OC1 cells (House Ear Institute) were cultured under permissive conditions (33°C, 10% CO₂) in high-glucose DMEM (Gibco BRL, 11,965,092) containing 10% FBS without antibiotics. Cells were transfected with plasmids using Lipofectamine PLUS (Invitrogen, 10,964-021) or Transporter™ 5 Transfection (Polysciences, 26,008-50) reagent, according to the manufacturer's instructions.

Chemicals

Bafilomycin A₁ (B1793), MG132 (M7449), and chloroquine (C6628) were obtained from Sigma.

Immunoblotting, immunoprecipitation, and immunofluorescence

Immunoblotting and immunofluorescence were performed as described previously [33,34]. Anti-OSBPL2 (Proteintech, 14,751-1-AP; and Novus, NBP1-92,236), anti-LC3 (Proteintech, 18,725-a-AP), anti-TUBB3/Tuj1 (BioLegend, 801,201), anti-MYO7A (Proteus, 25-6790), anti-NEFH/neurofilament-H (AB5539, Sigma), anti-CTSD (MA1-26,773, Invitrogen), anti-ACTB/β-actin (Santa Cruz Biotechnology, sc-1615), anti-HSPA5/BiP (ab21685), and anti-XBP1 (ab37151) were from Abcam, anti-MYC (2276S and 5605S), anti-DYKDDDDK (FLAG; 8146S and 2368S), anti-LC3A/B (4108S), anti-SQSTM1/p62 (5114S), anti-ubiquitin (3933S), anti-ERN1/IREα (14C10, 3294 T), anti-LAMP1 (9091S), anti-MTOR (7C10, 2983P), anti-phospho-MTOR (Ser2448; D9C2; 2971S), anti-phospho-PIK3CA/PI3K (C73F8; 4249S), anti-phospho-AKT (D9E; 4060S) were from Cell Signaling Technology, LysoTracker™ Red DND-99 (Invitrogen, L7528), and Alexa Fluor-conjugated phalloidin (Invitrogen, A12379) were from commercial sources. Immunoblotting was performed using primary antibodies at a 1:1,000 dilution, followed by corresponding anti-isotype secondary antibodies (Cell Signaling Technology, 7074P2 and 7076P2) at a 1:2,000 dilution. Signals were visualized using a SuperSignal West-Pico kit (Thermo Scientific, 34,579). Band intensities were quantified using ImageJ. Coimmunoprecipitation was performed using EZview Red Anti-FLAG M2 (Sigma, F2426) and anti-c-MYC Affinity Gel (Sigma, E6654). Immunofluorescence was detected in cultured cells using a blocking buffer containing 10% donkey serum (Sigma,

S30) and 1% bovine serum albumin (Affymetrix, 10,857) in phosphate-buffered saline (PBS; CellSTAR, CTB-PB1002-1). Free cholesterol was stained with 50 mg/ml of filipin (Sigma, F9765) in the blocking buffer for 2 h. The inner ear and brain tissues dissected from mice were fixed in 4% paraformaldehyde (PFA) in PBS at 4°C for 1 h. The fixed cochlea was permeabilized with 0.3% Triton X-100 (Biosesang, TR1020) and 0.3% saponin (Sigma, S4521) in PBS for 30 min and blocked with 5% goat serum (Sigma, S26) in PBS for 1 h at room temperature. Primary and fluorophore-tagged secondary antibodies were diluted 1:50 ~ 1:1,000 and 1:2,000, respectively. Confocal images were obtained using Carl Zeiss LSM700 or LSM780 microscopes while images were processed using ZEN software. Colocalization was measured using Manders' colocalization coefficients (MCC). To define overlapping signals above the 70-fluorescence threshold level, we used both green and red channels. Then, the average MCC was calculated from overlapping signals.

Animal experiments

The animal experimental protocols were reviewed and approved by the Institutional Animal Care and Use Committee at the Yonsei University College of Medicine (#2019-0250). All mice were handled following the Guidelines for the Care and Use of Laboratory Animals. Mice were housed under pathogen-free conditions with a light cycle from 7:00 AM to 7:00 PM and had *ad libitum* access to water and irradiated rodent chow (LabDiet, 0006972) or HFD (Research Diet, D12451). Rapamycin (Sigma, 37,094) was dissolved in DMSO (100 mg/ml) and stored at -20°C. Before use, rapamycin was diluted in a solution containing 5% PEG-400 (Sigma, 06855) and 5% Tween-80 (Sigma-Aldrich, P4780) as a stock solution (1.2 mg/ml). Mice in each group were intraperitoneally injected with a final dose of 2.0 mg/kg daily. The control mice were injected with the same amount of vehicle solution.

Generation of *osbpl2* knockout mice

Cas9 (New England Biolabs, M0386M), tagged with a nuclear localization signal, and gRNAs to target exon 3 of *Osbpl2* were purchased from MacroGen, Inc. (Seoul, Korea). gRNA activity (gRNA1: AATTAGTGGGATGATTGACTTGG, gRNA2: ACCAGCAAAAGTACTAGGAGTGG) was validated using *in vitro* cleavage reactions to knock out *Osbpl2*. Briefly, amplified *Osbpl2* was incubated for 90 min at 37°C with Cas9 (20 nM) and sgRNA (40 nM) in 1× NEB 3.1 buffer. Reactions were stopped with a 6× stop solution containing 30% glycerol, 1.2% SDS, and 100 mM EDTA. Cleavage activity was confirmed using electrophoresis.

osbpl2 knockout mice were generated by MacroGen, Inc. Briefly, mare's serum gonadotropin (7.5 IU) and human CGB (chorionic gonadotropin; 5 IU; Daesung Microbiological Labs, Daesung HCG) were administered to C57BL/6 N female mice. After 48 h, these female mice

were mated with C57BL/6 N stud male mice. The next day, virginal plug-checked female mice were sacrificed, and fertilized embryos were harvested. A sgRNA and Cas9 mixture was microinjected into one-cell embryos. Microinjected embryos were incubated at 37°C for 1–2 h. Approximately 14–16 injected one-cell embryos were transplanted into the oviducts of pseudo-pregnant recipient mice (ICR). After the F0 generation was born, genotyping of tail cut samples was performed via PCR (forward: GGGTTTGCACACTTGTTC, reverse: TCATGGACTAGCATGGGTCA) and T7E1 assay. T7E1-positive samples were subjected to TA Cloning and analyzed via Sanger sequencing. The following primers were used for the F1 generation genotyping: forward, TCTATAGGGGAATTTTCAGAGGC; reverse, GCGTACC TGTGCTTTTGAATTC.

Generation of transgenic mice

Transgenic mice were generated by MacroGen, Inc. cDNA encoding 3XFLAG-tagged wild-type or p.Q53Rfs*100 OSBPL2 was subcloned into the pCAGGS vector (Riken, RDB08938), which contains a chicken *ACTB*/β-actin promoter, between AvrII and PvuI restriction sites. The backbone fragment (~1.6 kb) was deleted through gel extraction, and ~4.7 kb fragment was microinjected into one-cell embryos. Precisely 4 ng/μl DNA was directly injected into the male pronucleus of the zygote using a micromanipulator. After the F0 generation was born, genotyping for the presence of the transgene was performed using tail cut samples via PCR (forward: CTGTGCGGAGCCGAAATCTG, reverse: ATGGTCCACACGCTGAAGTCGC). The target fragment size was 643 bp.

ABR

ABR thresholds were measured in a sound-proof chamber using Tucker-Davis Technologies (TDT) RZ6 digital signal processing hardware and BioSigRZ software (Alachua, FL, USA). Sub-dermal needles (electrodes) were positioned at the vertex, ventrolateral to the right and left ears of anesthetized mice. A calibrated click stimulus (10 μs) or tone burst stimuli (5 ms) were produced at 4, 6, 8, 10, 12, 18, 24, 30, and 42 kHz using SigGenRZ software and an RZ6 digital signal processor and were delivered to the ear canal using a multi-field 1 (MF1) magnetic speaker (TDT). Stimulus intensity was increased from 10 to 95 dB SPL in 5 dB steps. The ABR signals were fed into a low-impedance Medusa Biological Amplifier System (RA4LI, TDT), which delivered the signal to the RZ6 digital signal processing hardware. Recorded signals were filtered using a 0.5–1 kHz band-pass filter, and the ABR waveforms in response to 512 tone bursts were averaged. ABR thresholds for each frequency were determined using BioSigRZ software. Peak amplitudes (mV) were calculated using the waveform signal of the click-evoked ABRs as input/output (I/O) functions with an increasing stimulus level (20–90 dB SPL).

DPOAE

DPOAE was measured using a combination of TDT microphone-speaker systems. Primary stimulus tones were produced using an RZ6 digital signal processor with SigGenRZ software and delivered using a custom probe with an ER 10B+ microphone (Etymotic, IL, USA) and MF1 speakers positioned in the ear canal. Primary tones were set at a frequency ratio (f_2/f_1) of 1.2 with target frequencies of 6, 12, 16, 18, 22, 24, and 30 kHz. The f_2 intensity was the same as the f_1 intensity ($L_1 = L_2$). The sounds resulting from the primary tones were received via the ER 10B+ microphone and recorded using an RZ6 digital signal processor. The DPOAE input/output (I/O) functions were determined at specific frequencies (6 and 30 kHz) with an f_2/f_1 of 1.2, $L_1 = L_2$. The intensity of the primary tones was increased from 20 to 80 dB SPL in 5 dB SPL increments. Fast Fourier Transform was performed for each primary tone using DP-grams and for the I/O function intensity using BioSigRZ software to determine the average spectra of the two primaries, 2 f_1 - f_2 distortion products, and noise floors.

SEM

Inner ears were dissected and fixed in 2% paraformaldehyde with 2.5% glutaraldehyde in 0.1 M sodium cacodylate buffer (pH 7.4) for 2 h at room temperature. After fixation, the cochlear epithelium and tectorial membrane were separated and fixed overnight at 4°C with 2.5% glutaraldehyde in 0.1 M sodium cacodylate buffer (pH 7.4) containing 2 mM calcium chloride and 3.5% sucrose. The fixed samples were washed three times in 0.1 M sodium cacodylate buffer with 2 mM calcium chloride for 20 min at 4°C and then post-fixed using an osmium tetroxide (OsO_4)-thiocarbohydrazide (OTO; Polysciences, 02236). Samples were dehydrated using a graded ethanol series, dried using a critical point dryer (Leica EM CPD300, Wetzlar, Germany), fixed on a stub (Agar Scientific, AGG301-S-50), and coated with platinum (20–30 nm) using a sputter coater (ACE600; Leica Microsystems). The platinum-coated specimens were mounted on a stub holder and imaged using a Schottky emission scanning electron microscope (JSM-IT500, JEOL, Tokyo, Japan).

TEM

Cochleae were fixed in 2% paraformaldehyde with 2% glutaraldehyde in 0.1 M phosphate buffer (pH 7.4) for 12 h, washed with 0.1 M phosphate buffer, post-fixed with 1% OsO_4 in 0.1 M phosphate buffer for 2 h, dehydrated using ethanol series, and infiltrated with propylene oxide (Fisher scientific, 10,562,351) for 10 min. Specimens were embedded with a Poly/Bed 812 kit (Polysciences, 08792-1) and polymerized in an electron microscope oven (TD-700, DOSAKA, Japan) at 65°C for 12 h. The tissue block was cut into 200-nm semi-thin sections using an ultramicrotome equipped with a diamond knife and stained with toluidine blue for optical microscope observation. The region of interest was then cut into 80-nm sections using the ultramicrotome, placed on copper grids (EMS, EMS300-Cu), double stained with 3% uranyl acetate for 30 min and 3% lead citrate for 7 min, and imaged using

a transmission electron microscope (JEM-1011, JEOL, Tokyo, Japan) equipped with a Megaview III CCD camera (Soft imaging system-Germany) at an acceleration voltage of 80 kV.

Identification of WT and mutant OSBPL2 interactors

Proteins (75 mg) extracted from HEK 293 cells expressing p3XFLAG-OSBPL2 WT, p.Q53Rfs*100, or bacterial alkaline phosphatase were incubated with 80 μl of FLAG M2 agarose beads (Sigma, A2220) for 48 h at 4°C in an orbital shaker. The agarose beads were washed four times with lysis buffer to restrict nonspecific binding. Subsequently, 200 μl of an elution buffer containing 150 ng/ μl 3xFLAG peptide (Sigma, F4799) was added, and the samples were incubated overnight. The eluates were analyzed using immunoblotting, Coomassie Brilliant Blue staining, and silver staining. The eluates were digested and subjected to NanoLC-MS/MS analysis. Peptides were separated on a C18 precolumn (75 $\mu\text{m} \times 2$ cm, nanoViper, Acclaim PepMap100; Thermo Fisher Scientific, 164,946) and analytical C18 column (75 $\mu\text{m} \times 50$ cm, PepMap RSLC; Thermo Fisher Scientific, 164,567). Peptides were analyzed using an LC-MS/MS system consisting of an Easy nLC 1000 (Thermo Fisher Scientific, LC120) and an Orbitrap Fusion Lumos mass spectrometer (Thermo Fisher Scientific) equipped with a nano-electrospray source. MS/MS spectra were analyzed against the Uniprot human database using the following software analysis protocol. The reversed sequences of all proteins were appended into the database for the FDR calculation. ProLucid was used to identify the peptides, with a precursor mass error of 5 ppm and a fragment ion mass error of 200 ppm [35]. The output data files were filtered and sorted to compose the protein list using DTASelect (The Scripps Research Institute, CA, USA), with two and more peptide assignments for protein identification and a false positive rate less than 0.01 [36]. The mass spectrometry proteomics data were deposited to the ProteomeXchange Consortium using the PRIDE partner repository (dataset identifier PXD021514).

Novel object recognition

The memory test was performed via novel object recognition test. Mice were controlled in square test boxes (40 x 40 x 35 cm) for recognition trials. A red-painted quadrangular pyramid and a green-painted cylinder were used as objects. Mice were handled for 2 days. Mice were allowed to explore the empty test box for 20 min on day 1. After 24 h, object recognition test was conducted. Following a 5-min customization phase, two equal objects were placed in the box and the mouse was allowed to explore the objects for 10 min. After 1 h, the novel object trail was conducted. Following a 5 min customization phase, two different objects (old and novel) were placed in the box and test was conducted equally. Object interaction was defined as valid whenever a mouse's head was within 2 cm of the object and directed toward the object. Novel object interaction (%) was calculated as follows: (novel object interaction x 100)/(old object interaction + novel object interaction).

CTSD activity assay

The enzyme activity of CTSD was determined using a fluorometric assay kit according to the manufacturer's protocol (Abcam, ab65302). HEK 293 cell lysates (1×10^6) were homogenized quickly by pipetting up and down a few times and centrifuged at $200 \times g$ for 5 min at 4°C . The cell pellet was resuspended in 200 μl of chilled cell lysis buffer and centrifuged for 5 min at 4°C at top speed. The samples were used for an enzymatic assay. Proteins were incubated at 37°C for 1 h with GKPIILFFRLK(Dnp)-D-R-NH₂ labeled with MCA (CTSD substrate) and protected from light. After incubation for 1 h, fluorescence signal intensity was measured using a fluorescence microplate reader (Varioskan Flash 3001; Thermo Fisher Scientific, 5,250,040) at an excitation/emission of 328/460 nm.

Lipid levels in inner ear and brain tissues

Lipid levels were measured using total cholesterol and triglyceride assay kit (BIOMAX, BM-CHO-100 and BM-TGR-100). Approximately 10–20 mg of inner ear and brain tissues were homogenized in chloroform-isopropanol- Triton X-100 (Sigma, 372,978 and 278,475,) solution (7:11:0.1) for total cholesterol extraction and in distilled water-5% Triton X-100 solution for triglyceride extraction. Each sample was measured using a fluorescence microplate reader at an excitation/emission of 535/590 nm.

GO analysis

The interactors of WT and p.Q53Rfs*100 OSBPL2 were analyzed using the Database for Annotation, Visualization and Integrated Discovery (DAVID) for functional annotation. The Functional Annotation Tool in the online version of DAVID (version 6.8) was run (<http://david.abcc.ncifcrf.gov/>) using the default parameters. GO categories representing molecular function, cellular component, and biological process were separately analyzed for enrichment. p -value < 0.05 was considered significant.

Acknowledgments

We thank the participating families for their contributions. We also thank Yonsei Advanced Imaging Centre in cooperation with Carl Zeiss Microscopy and the National Biobank of Korea, Centers for Disease Control and Prevention, Republic of Korea (4845-301, 4851-302 and -307).

Funding

This study was supported by the Yonsei University College of Medicine (Team Science Award 6-2021-0003 to H.Y.G. and 6-2021-0002 to J.J.), by the National Research Foundation of Korea (NRF) (2021R1A2C2003549 and 2018R1A5A2025079 to H.Y.G., 2020R1A2C3005787 to J.Y.C., 2019R1A2C1084033 to J.J. and Korea Mouse Phenotyping Project 2020M3A9D5A01082439 to H.Y.G.), and by the Ministry of Health and Welfare (2017M3A9E8029714).

Statistical analysis

All quantitative data were obtained from at least three independent experiments. Statistical differences between two groups were examined using Student's t -test or two-way analysis of variance (ANOVA) with

Bonferroni correction for multiple comparisons using the GraphPad Prism 7.0 software (GraphPad Software, CA, USA). Two-sided p values of less than 0.05 were considered significant.

Disclosure statement

No potential conflict of interest was reported by the author(s).

Data availability statement

The datasets used and/or analyzed during the current study are available from the corresponding author on request.

ORCID

Heon Yung Gee  <http://orcid.org/0000-0002-8741-6177>

References

- [1] Dror AA, Avraham KB. Hearing loss: mechanisms revealed by genetics and cell biology. *Annu Rev Genet.* 2009;43:411–437.
- [2] Cunningham LL, Tucci DL. Hearing loss in adults. *N Engl J Med.* 2017;377:2465–2473.
- [3] Livingston G, Sommerlad A, Orgeta V, et al. Dementia prevention, intervention, and care. *Lancet.* 2017;390:2673–2734.
- [4] Lin FR, Ferrucci L. Hearing loss and falls among older adults in the United States. *Arch Intern Med.* 2012;172:369–371.
- [5] Mener DJ, Betz J, Genter DJ, et al. Hearing loss and depression in older adults. *J Am Geriatr Soc.* 2013;61:1627–1629.
- [6] Goman AM, Reed NS, Lin FR. Addressing estimated hearing loss in adults in 2060. *JAMA Otolaryngol Head Neck Surg.* 2017;143:733–734.
- [7] Xing G, Yao J, Wu B, et al. Identification of OSBPL2 as a novel candidate gene for progressive nonsyndromic hearing loss by whole-exome sequencing. *Genet Med.* 2015;17:210–218.
- [8] Wu N, Husile H, Yang L, et al. A novel pathogenic variant in OSBPL2 linked to hereditary late-onset deafness in a Mongolian family. *BMC Med Genet.* 2019;20:43.
- [9] Thoenes M, Zimmermann U, Ebermann I, et al. OSBPL2 encodes a protein of inner and outer hair cell stereocilia and is mutated in autosomal dominant hearing loss (DFNA67). *Orphanet J Rare Dis.* 2015;10:15.
- [10] Lehto M, Laitinen S, Chinetti G, et al. The OSBP-related protein family in humans. *J Lipid Res.* 2001;42:1203–1213.
- [11] Hynynen R, Suchanek M, Spandl J, et al. OSBP-related protein 2 is a sterol receptor on lipid droplets that regulates the metabolism of neutral lipids. *J Lipid Res.* 2009;50:1305–1315.
- [12] Wang H, Ma Q, Qi Y, et al. ORP2 delivers cholesterol to the plasma membrane in exchange for phosphatidylinositol 4, 5-bisphosphate (PI(4,5)P(2)). *Mol Cell.* 2019;Vol. 73:458–73.e7.
- [13] Escajadillo T, Wang H, Li L, et al. Oxysterol-related-binding-protein related protein-2 (ORP2) regulates cortisol biosynthesis and cholesterol homeostasis. *Mol Cell Endocrinol.* 2016;427:73–85.
- [14] Yao J, Zeng H, Zhang M, et al. OSBPL2-disrupted pigs recapitulate dual features of human hearing loss and hypercholesterolaemia. *J Genet Genomics.* 2019;46:379–387.
- [15] Wang H, Lin C, Yao J, et al. Deletion of OSBPL2 in auditory cells increases cholesterol biosynthesis and drives reactive oxygen species production by inhibiting AMPK activity. *Cell Death Dis.* 2019;10:627.
- [16] Paulson HL. Protein fate in neurodegenerative proteinopathies: polyglutamine diseases join the (mis)fold. *Am J Hum Genet.* 1999;64:339–345.
- [17] Gee Heon Y, Noh Shin H, Tang Bor L, et al. Rescue of ΔF508 -CFTR trafficking via a grasp-dependent unconventional secretion pathway. *Cell.* 2011;146:746–760.
- [18] Dubnikov T, Ben-Gedalya T, Cohen E. Protein quality control in health and disease. *Cold Spring Harb Perspect Biol.* 2017;9:a023523.

- [19] Jung J, Kim J, Roh SH, et al. The HSP70 co-chaperone DNAJC14 targets misfolded pendrin for unconventional protein secretion. *Nat Commun.* 2016;7:11386.
- [20] Choi HJ, Lee HJ, Choi JY, et al. DNAJC14 ameliorates inner ear degeneration in the DFNB4 Mouse Model. *Mol Ther Methods Clin Dev.* 2020;17:188–197.
- [21] Bae SH, Robertson NG, Cho HJ, et al. Identification of pathogenic mechanisms of COCH mutations, abolished cochlin secretion, and intracellular aggregate formation: genotype-phenotype correlations in DFNA9 deafness and vestibular disorder. *Hum Mutat.* 2014;35:1506–1513.
- [22] Jung J, Kim HS, Lee MG, et al. Novel COCH p.V123E mutation, causative of dfna9 sensorineural hearing loss and vestibular disorder, shows impaired cochlin post-translational cleavage and secretion. *Hum Mutat.* 2015;36:1168–1175.
- [23] Jung J, Lee JS, Cho KJ, et al. Genetic predisposition to sporadic congenital hearing loss in a pediatric population. *Sci Rep.* 2017;7:45973.
- [24] Rim JH, Noh B, Koh YI, et al. Differential genetic diagnoses of adult post-lingual hearing loss according to the audiogram pattern and novel candidate gene evaluation. *Hum Genet.* 2021; DOI:10.1007/s00439-021-02367-z.
- [25] Oh KS, Walls D, Joo SY, et al. COCH-related autosomal dominant nonsyndromic hearing loss: a phenotype-genotype study. *Hum Genet.* 2021; DOI:10.1007/s00439-021-02368-y.
- [26] Sánchez-Martín P, and Komatsu M. - steering the cell through health and disease. *J Cell Sci.* 2018;131:jcs222836.
- [27] Conlon B, Langguth B, and Hamilton C, et al. Bimodal neuromodulation combining sound and tongue stimulation reduces tinnitus symptoms in a large randomized clinical study. *Sci Transl Med.* 2020;12:eabb2830.
- [28] Freeman S, Mateo Sánchez S, Pouyo R, et al. Proteostasis is essential during cochlear development for neuron survival and hair cell polarity. *EMBO Rep.* 2019;20:e47097.
- [29] Fu X, Sun X, Zhang L, et al. Tuberous sclerosis complex-mediated mTORC1 overactivation promotes age-related hearing loss. *J Clin Invest.* 2018;128:4938–4955.
- [30] Ye B, Wang Q, Hu H, et al. Restoring autophagic flux attenuates cochlear spiral ganglion neuron degeneration by promoting TFEB nuclear translocation via inhibiting mTOR. *Autophagy.* 2019;15:998–1016.
- [31] Ebrahimi-Fakhari D, Saffari A, Wahlster L, et al. Congenital disorders of autophagy: an emerging novel class of inborn errors of neuro-metabolism. *Brain.* 2015;139:317–337.
- [32] Esposito A, Falace A, Wagner M, et al. Biallelic DMXL2 mutations impair autophagy and cause Ohtahara syndrome with progressive course. *Brain.* 2019;142:3876–3891.
- [33] Gee HY, Tang BL, Kim KH, et al. Syntaxin 16 binds to cystic fibrosis transmembrane conductance regulator and regulates its membrane trafficking in epithelial cells. *J Biol Chem.* 2010;285:35519–35527.
- [34] Son EJ, J-h M, Ankamreddy H, et al. Conserved role of sonic hedgehog in tonotopic organization of the avian basilar papilla and mammalian cochlea. *Proceedings of the National Academy of Sciences of the United States of America* 2015; 112:3746–3751.
- [35] Xu T, Park SK, Venable JD, et al. ProLuCID: an improved SEQUEST-like algorithm with enhanced sensitivity and specificity. *J Proteomics.* 2015;129:16–24.
- [36] Tabb DL, McDonald WH, and Yates JR, 3rd. DTASelect and Contrast: tools for assembling and comparing protein identifications from shotgun proteomics. *J Proteome Res.* 2002;1:21–26.